FABRICATION, CHARACTERIZATION AND SIMULATION OF PLASMONIC CAVITIES

A THESIS

SUBMITTED TO THE DEPARTMENT OF PHYSICS

AND THE INSTITUTE OF ENGINEERING AND SCIENCE

OF BILKENT UNIVERSITY

IN PARTIAL FULFILLMENT OF THE REQUIREMENTS

FOR THE DEGREE OF

MASTER OF SCIENCE

By

Mustafa Karabıyık

October, 2010

I certify that I have read this thesis and that in my opinion it is fully adequate, in scope and in quality, as a thesis for degree of Master of Science.

Prof. Atilla Aydınlı (Advisor)

I certify that I have read this thesis and that in my opinion it is fully adequate, in scope and in quality, as a thesis for degree of Master of Science.

Assist. Prof. Dr. Coşkun Kocabaş

I certify that I have read this thesis and that in my opinion it is fully adequate, in scope and in quality, as a thesis for degree of Master of Science.

Assist. Prof. Dr. Emrah Özensoy

Approved for the Institute of Engineering and Science

_____

Prof. Dr. Levent Onural

(Director of the Institute)

ABSTRACT

FABRICATION, CHARACTERIZATION AND SIMULATION OF PLASMONIC CAVITIES

Mustafa Karabıyık

M.S. in Department of Physics

Supervisor: Prof. Dr. Atilla Aydınlı

November, 2010

Surface plasmon polaritons (SPPs) originate from the collective oscillations of conduction electrons coupled with photons propagating at metal-dielectric interfaces. A uniform metallic gratings change the dispersion (energy-momentum relation) of a flat metal surfaces due to the interaction of SPPs with the periodic structure. By breaking the symmetry of the periodic plasmonic structure, SPP cavities can be achieved and SPPs can be localized inside the cavity regions. The aim of this thesis is to understand the physics of phase shifted grating based plasmonic cavities. To this end, we fabricated uniform gratings and phase shifted gratings using electron beam lithography, and optically characterized these SPP structures with polarization dependent reflection spectroscopy. We verified experimental results with numerical simulations SPP propagation and localization on the grating structures. Dispersion curves of SPPs have been calculated by solving Maxwell's wave equations using finite difference time domain method (FDTD) with appropriate boundary conditions in agreement with experimentally obtained data. We studied the dispersion curve as a function of grating profile modulation where we vary the ridge height and width of the ridges. We find that the plasmonic band gap width increases as the ridge height of the ridges in the grating increases. Optimum duty cycle of grating to observe plasmonic band gap is determined to be half of the grating period. Amount of the phase shift added to the periodicity of the uniform grating defines the energy of the cavity state, which is

periodically related to the phase shift. A plasmonic cavity with a quality factor 80 has been achieved. The propagation mechanism of SPPs on coupled cavities is plasmon hopping from a given cavity to the next one.

Keywords: Surface plasmon polaritons, Uniform gratings, Phase shifted gratings, Cavity, Localization, Cavity-cavity coupling.

ÖZET

PLAZMONİK KOVUKLARIN ÜRETİMİ, KARAKTERİZASYONU VE BENZETİMİ

Mustafa Karabıyık
Fizik Bölümü, Yüksek Lisans
Tez Yöneticisi: Prof. Dr. Atilla Aydınlı
Kasım, 2010

Yüzey plazmon polaritonları metal-dielektrik yüzeyinde elektron ve foton çiltlenmasiyle oluşan elektromanyetik dalgalanmalardır. Düzgün kırınım ağları, plazmonların periyodik yapıyla etkileşimine bağlı olarak, plazmonların enerji-momentum özelliklerini düz metal yüzeylere nisbeten değiştirirler. Periyodik yapının simetrisini kırarak plazmonların yerelleşmesi sağlanabilir. Bu tezin amacı, faz kaymalı kırınım ağı tabanlı plazmonik kovukların fiziğini anlamaktır. Bu amaçla, elektron demet litografisi ile düzgün kırınım ağlı ve faz kaymalı kırınım ağlara dayanan plazmonik yapılar oluşturuldu ve oluşturulan yapılar polarizasyona bağımlı yansıma ölçümleriyle karakterize edildi. Deneysel sonuçlar, plazmonik yapıların benzeşimi ile doğrulandı. Enerji-momentum eğrileri, Maxwell denklemlerini zamana bağımlı sonlu farklar yöntemini çözerek hesaplandı ve sonuçların deneysel sonuçlarla uyumlu olduğu görüldü. Düzgün kırınım ağının profiline bağlı olarak, enerji momentum eğrilerini çalıştık. Düzgün kırınım ağının derinl, bant aralığı sönümlenmesi için uygun değeri periyodun yarısıdır. Düzgün kırınım ağının derinliği arttıkça bant aralığının genişliği de artar. Düzgün kırınım ağınına eklenen faz kaymasının miktarı kovuğun enerjisini belirler ve kovuğun enerjisi faz kaymasına bağımlı olarak periyodiktir. Kalite faktörü 80 olan plazmonik kovuklar elde edildi. Plazmonların hareket mekanizması bir kovuktan diğerine hoplama mekanizmasıyla gerçekleştiği anlaşıldı.

Anahtar sözcükler: Yüzey plazmon polaritonları, Düzgün kırınım ağları, Fazı kaymış kırınım ağları, Kovuk, Yerelleşme, Kovuk-kovuk eşlesmesi.

Acknowledgements

I am thankful to my academic advisor Prof. Atilla Aydınlı for his guidance and advices.

I am thankful to Dr. Sinan Balcı about his help, advice, collaboration, guidance and contribution and reviewing of this thesis.

I would like to thank to Assist. Prof. Coşkun Kocabaş for his ideas, guidance and collaboration.

I would like to thank to Prof. Dr. Raşit Turan, Urcan Güler and Seçkin Öztürk for their help, training and discussions about electron beam lithography at METU Central Laboratory.

I would like to thank to my group members Dr. Ömer Salihoğlu, Ertuğrul Karademir, Sinan Gündoğdu, and Bektaş Akyazı for discussions and friendship.

I would like to thank to my old group members Servet seçkin Şenlik, Dr. Aşkın Kocabaş, İmran Akca and Samet Yumrukçu.

I wish to express my special thanks to my family and friends for their support and love.

I wish to express my love to my wife Emine who has always been near me for support.

to my parents and my wife

Contents

1. Introduction.....1

2. Surface Plasmon Polaritons.....6

2.1. Optical Properties of Metals.....6

2.2. Fundamentals of SPPs.....12

2.3. Propagation of SPPs on Periodic Surface.....23

2.4. Localization of SPPs.....26

2.5. Simulation of SPP propagation on Plasmonic Structures.....28

3. Fabrication and Characterization of Plasmonic Structures.....32

3.1. Fabrication of SPP Structures Using Electron Beam Lithography.....32

3.1.1. Fabrication of Uniform Gratings.....38

3.1.2. Fabrication of Phase Shifted Gratings.....39

3.2. Optical Characterization of SPP Structures Using Supercontinuum Light Source.....40

4. Phase Shifted Grating Based Plasmonic Band Gaps and Cavities.....42

4.1. Uniform Grating Based Plasmonic Band Gap.....43

4.2. Phase Shifted Grating Based Plasmonic Band Gaps and Cavities.....52

4.3. SPP Propagation Mechanism on Coupled Phase Shifted Gratings.....59

5. Conclusions and Suggestions.....65

List of Figures

Figure 2.1: Real part, ε_1 and imaginary part, ε_2 for silver calculated from Drude model and experimentally extracted data by Palik [54].....9

Figure 2.2: a) Schematic density of states for the 3d and 4s bands of a transition for copper. b) Reflectivity of copper. [33].....10

Figure 2.3: Refractive indices, n and absorption coefficients, κ for silver calculated from Drude model and compared with experimentally extracted data by Palik[54].....12

Figure 2.4: Electric field intensity profile of a SPP propagating at the metal dielectric interface.....13

Figure 2.5: Surface plasmon polariton dispersion relation for silver-air interface and dispersion of light in air. Dispersion of SPP is calculated with the Drude model as represented in the inset [13].....16

Figure 2.6: Electric and magnetic field distributions of SPPs propagating at the metal-dielectric interface.....17

Figure 2.7: Cross section view from the x-z plane, of electric and magnetic field distributions of SPP propagation at the metal-dielectric interface.....17

Figure 2.8: Schematic representations of (a) grating coupler and (b) prism coupler (c) near field fiber coupler.....20

Figure 2.9: Illustration of momentum mismatch between the surface plasmon polariton and light superimposed on the long wavelength part of the dispersion curve.....22

Figure 2.10: Standing wave profiles of a) light in photonic crystal, and b) SPP on the periodic surface.....24

Figure 2.11: Electric field distributions for a) ω^+ and b) ω^- modes.....24

Figure 2.12: Schematic representation of dispersion relation of SPPs for the uniform metallic grating and flat metal.....25

Figure 2.13: Envelope of electric field intensity distribution of SPP excited in a localized cavity state on a SBM, with phase shift of π.....27

Figure 2.14: Dispersion relation of SPPs for the metallic gratings with a cavity. Note the cavity state in the band gap.....27

Figure 2.15: Simulation window for SPP mode source configuration using Lumerical software. Inset: Electric field intensity distribution of a plasmonic mode at the metal-air interface calculated by the source.....30

Figure 2.16: Simulation window for plane wave source configuration used to calculate the dispersion relation of the plasmonic structure.....30

Figure 3.1: Schematic representation of bi-layer undercut process.....35

Figure 3.2: A photograph of a sample taken by the optical microscope which is partially lifted off.....36

Figure 3.3: SEM image of a SBM that has partially lifted off parts.....37

Figure 3.4: Top view SEM image of a uniform grating fabricated by e-beam lithography with a period of 440 nm.....39

Figure 3.5: Top view SEM image of a SBM fabricated by e-beam lithography with a period of 440 nm.....40

Figure 3.6: Schematic representation of an ellipsometer set up for reflection measurements.....41

Figure 4.1: SEM image of a uniform grating with a period of 420 nm.....45

Figure 4.2: Dispersion of SPPs for the uniform grating with a period of 420 nm measured by reflectometer in the bound SPP mode regime.....45

Figure 4.3: Dispersion of SPPs for the uniform grating with a period of 400 nm calculated in the bound SPP mode regime.....47

Figure 4.4: Width of the Reflection spectra of a uniform square grating with a period of 400 nm, SPP modes are excited at a 44.7^0 incidence angle and incident wavelength is varied.....47

Figure 4.5: Electric field intensities and directions for a) ω+ and ω-.....48

Figure 4.6: Schematic representation of a uniform square grating, a is the period, h is the ridge height, d is the ridge width and d/a is the duty cycle.....48

Figure 4.7: Modulation of plasmonic band gap with grating ridge height.....49

Figure 4.8: Graph of extinction vs. incident photon wavelength.....51

Figure 4.9: Graph of duty cycle vs. extinction depth.....51

Figure 4.10: SEM image of a SBM with a period of 410 nm.....54

Figure 4.11: Dispersion for the SBM with a period of 410 nm measured by ellipsometer.....54

Figure 4.12: Dispersion for the uniform grating with a period of 400 nm calculated.....55

Figure 4.13: Electric field intensity distribution of SPPs excited on a SBM with phase shifts of π.....56

Figure 4.14: FDTD calculated electric field intensity distribution of SPPs excited on a SBM with phase shifts of π, 3π and 5π from top to bottom, respectively.....56

Figure 4.15: Extinction data for SBMs with a phase shift of δ a) a/2 times period b) 3a/2 times period b) -3a/10 times period b) 7a/10 times period.....58

Figure 4.16: Graph of 2π times phase shift divided by period vs. cavity state.....57

Figure 4.17: (a) Schematic side view of a cavity structure with a phase shift of δ. (b) Schematic side view of a sampled Bragg mirror (SBM) consisting of coupled SPP cavities.....60

Figure 4.18: (a) Fast Fourier transform of the profile of the unperturbed grating. (b) Fast Fourier transform of the profile of the SBM. (c) Reflectivity of a silver grating that has silver ridges with a period a=400 nm, a line width=200 nm, a line height=30 nm. (d) Reflectivity of a silver SBM of silver ridges with a period a=400 nm, line width=200 nm, line height=30 nm.....60

Figure 4.19: (a) Dispersion of SBM cavity that has 10 ridges in between each phase shift region. (b) Dispersion of SBM that has 30 grating lines in between each phase shift region.....62

Figure 4.20: (a) Electromagnetic modes supported by cavities with a phase at every 10 ridges. Note the coupling of the cavities. (b) Electromagnetic modes supported by cavities with a phase shift at every 30 ridges.....63

Chapter 1

1. Introduction

Interest in plasmonics has been renewed with the recent development of nanofabrication techniques. Nowadays, plasmonics is one of the most studied topics in physics. As the properties of surface plasmons are being studied many new properties have are being discovered suggesting interesting applications.

Excitation of surface plasmons with light leads to formation of surface plasmon polaritons, SPPs, a hybrid particle composed of charge oscillations coupled to electromagnetic waves. SPPs and localized SPPs were described at the beginning of 20^{th} century in a mathematical description that was given in the context of radio waves propagating along the surface of a conductor [1, 2]. Reflection of visible light from metallic gratings resulting in anomalous intensity drops in the reflection spectra was discovered by Wood and known as the "Woods anomaly". This phenomenon was then explained within the theoretical framework of Fano [3]. Diffraction of electrons from thin metallic foils described the idea of loss at metallic films [4] and work on diffraction gratings in the optical region was also added to the description. Excitation of SPPs with visible light using prism coupling was

accomplished by Kretschmann and Raether [5]. In the following years, SPP as a tool in technology has found a wide area of applications. Plasmonics enables the study of subwavelength optics below the diffraction limit and guiding of light in the subwavelength regime [6] while optical devices cannot reach beyond the diffraction limit [7]. Massive localized electric fields of surface plasmons are used to enhance the weak Raman signals, [8]. Using surface plasmon enhancement even a single molecule can be detected on plasmonic surfaces [9]. As a result, recently, plasmons have attracted great attention for applications in chemical and biological sensors [10]. Plasmonic lasers have also been demonstrated [11]. These results suggest that plasmonics is a multi disciplinary research field.

Surface plasmon polaritons can be classified into two types, as propagating and localized. Localized SPPs involve non-propagating excitation of conduction electrons of metal nanoparticles coupled to the photons. These modes are created by the coupling of photons to conduction electrons in small subwavelength metal nanoparticles. Mie developed the theory of the scattering and absorption of photons from small spheres [12]. Curved surface area of the particle exerts an effective restoring force on the driven electrons so that resonance can arise [13]. Localized plasmon resonance can be excited by illuminating light directly onto the metal nanoparticles whereas propagating SPPs require special phase matching techniques. Shape, size and material of nanoparticles define the optical properties of nanoparticles. Solution phase synthesis and electron beam lithography are two common methods to obtain metal nanoparticles [14, 15]. By tuning the size of nanoparticle for constant shape and material, desired optical properties in transmission and reflection can be obtained.

Decorations recovered from fourth A.D. appear red in transmission and green in reflection due to plasmons since nanoparticles were embedded into the glass matrix. El-Sayed et.al used gold nanoparticles with desired optical properties for surface

plasmon resonance biosensors to detect living whole cells. By marking the cancer cells with gold nanoparticles and measuring absorption of nanoparticles from tissues, they were able to image the cancer type cells [16]. A different field of study is the light emitting diode (LED) technology. InGaN light emitting diodes have been commercially available. Light emitting diodes are being considered to be used in solid-state lighting systems instead of light bulbs. However, there is intense work to improve and enhance emission of light from InGaN LEDs. Okomato et.al described a method to enhance emission efficiency through energy transfer between quantum wells and surface plasmons [17]. Surface plasmons can increase the density of states which leads to increased spontaneous emission rates in the semiconductor leading to the enhancement of light emission due to surface plasmon-quantum well coupling. A similar concept is used to increase the solar cell efficiency [18]. Ebbessen et.al reported the enhancement of surface plasmon transmission through subwavelength holes which leads to wavelength-selective transmission with efficiencies of about 1000 times higher than expected [19]. Furthermore, light localized in the subwavelength regime guided in a linear chain of spherical metal nanoparticles was achieved which can be used for subwavelength transmission in integrated optical circuits and for near-field optical microscopy. In such nanoparticle chains, light is transmitted by interparticle coupling [20]. The degree of subwavelength confinement was quantified by Kuipers et.al who showed that it is possible to squeeze light to dimensions 16 times smaller than their wavelength in vacuum with a taper structure i.e. it is possible to concentrate light with a wavelength of 1500 nm to a diameter smaller than 100 nm [21]. Light confinement to subwavelength dimensions makes it possible to image features that cannot be imaged by optical microscopes. Sub–diffraction imaging with 60 nm half-pitch resolution, or one-sixth of the illumination wavelength was achieved by Zhang et.al [22]. The propagation lengths of plasmons are in the micrometer scale in such structures due to absorption losses of the metal structures. The propagation

length of plasmons can be increased to millimeter scale with the use of metal-insulator-metal structures [23, 24].

Periodically layered photonic crystal structure that consists of two different refractive index materials, results in a photonic band gap in transmission of light through the photonic structure [25]. This analogy was applied to plasmons on metallic gratings resulting in a plasmonic band gap, plasmonic band gap represents that there are no plasmonic modes supported by the system at an energy interval [26]. Optical cavities are obtained by breaking the symmetry of the photonic crystal [27]. High transmission bands at frequencies within the band gap of the unperturbed photonic crystal can be created resulting in the localization of light within the cavity region [28]. This analogy was also applied to plasmon as phase shifted metallic gratings that results in a plasmonic cavity state within the band gap of the uniform metallic grating [29]. Localization of propagating SPPs may also find wide range of applications in technology [30]. Moiré surface is a special kind of one dimensional biharmonic grating which has a superperiod obtained by adding two periodicities that are close to each other. It is used to localize SPPs, since these structures contain a phase shift element in the superperiodicity [31]. Phase shifts in Moiré structures are π (half of the period) and the amount of phase shift is constant. Another way to achieve plasmonic localization is perturbing the effective index of the SPPs on periodic medium by periodically loading the surface with a specific dielectric [32]. Energy of the cavity state thus created is sensitive to dielectric thickness, type and length.

In this work, we study the properties of SPPs in the plasmonic band gap cavities on uniform gratings and phase shifted gratings. Experimental and simulation results of SPP structures are given and compared. The role of grating ridge height on the plasmonic band gap properties has been studied. We also studied the effect of ridge width on the plasmonic band gap. Energy of the cavity state within the band gap by

varying the phase shift is identified. By changing the periodicity and modulating the phase shift in the periodicity of the grating, energy of the desired cavity state can be tuned. Controlling the energy of the cavity state within the band gap and confinement of plasmons can have a wide range of applications. Our results imply possibilities of SPP based Bragg reflectors, emitters, and filters [30]. We use electron beam lithography to create periodic structures with phase shifts. Using electron beam lithography, we fabricate SPP structures and optically characterize them. We also simulate localization of SPPs in these cavities. We characterized two types of plasmonic structures i.e. metallic uniform grating surfaces and metallic phase shifted grating surfaces, both experimentally and numerically. Coupled cavities are also studied, SPP propagation along coupled cavities has been studied and properties of hopping mechanism properties are discussed. Dispersion profiles for coupled cavities are identified.

Chapter 2 describes optical properties of metals essential to understand surface plasmons, fundamentals of SPP physics, excitation of SPPs, and behavior of SPPs on flat, grating and phase shifted grating metallic surfaces. Simulations techniques of SPP structures are also discussed.

Chapter 3 gives information about fabrication and characterization of plasmonic structures. Fabricating SPP structures with the use of electron beam lithography and polarization dependent reflection measurements are explained.

Chapter 4 is about experimental and simulation results of SPP structures. Properties of plasmonic band gap on uniform gratings are given. Energy of the cavity state dependence upon phase shift in gratings and higher order plasmonic band gaps are explained. SPP propagation mechanism on coupled phase shifted gratings is explained.

In Chapter 5, conclusions and ideas for future directions are given.

Chapter 2

2. Theoretical Background

In order to understand the properties of SPPs on various surfaces, one needs to understand the optical response of the metals and dielectrics. This chapter gives a summary of optical properties of metals, field distribution, propagation distance and dispersion of SPPs. SPP excitation and SPPs in periodically structured metallic surfaces are discussed. Methods for SPP localization are identified. Simulations of SPP structures are summarized.

2.1. Optical Properties of Metals

In a wide range of frequencies, optical properties of metals can be explained by a plasma model. In this plasma model, a free electron gas moves against fixed positive ion cores. Electron-electron interactions are ignored. Response of the free electron gas to the applied electric field defines the optical properties of metals. Oscillation of electrons is damped due to electron-core collisions with a characteristic collision frequency $\gamma=1/\tau$ of the order of 100 THz, where τ is mean free time of free electron gas, which is of the order of 10^{-14} s at room temperature.

Equation of motion for an electron sea affected by an externally driven electric field can be written as

$$m\ddot{x} + m\dot{x}\gamma = -eE \tag{2.1}$$

where m is the mass of electron, e is fundamental charge of electron and E is the applied electric field. To solve this differential equation Eq. 2.1, $x(t)$ can be assumed as $x(t)=x_0e^{-iwt}$ which results in

$$x(t) = \frac{e}{m(w^2 + i\gamma w)}E(t) \tag{2.2}$$

Polarization (P) caused by electron displacement is $P=nex$ and can be expressed as

$$P = \frac{ne^2}{m(w^2 + i\gamma w)}E \tag{2.3}$$

The dielectric displacement is $D=\varepsilon_0E+P$ and can be expressed as

$$D = \varepsilon_0(1 - \frac{w_p^2}{w^2 + i\gamma w})E \tag{2.4}$$

where $w_p^2=ne^2/\varepsilon_0m$ is identified as the plasma frequency of the free electron gas. The dielectric function of the free electron gas can then be written as

$$\varepsilon(w) = 1 - \frac{w_p^2}{w^2 + i\gamma w} \tag{2.5}$$

The real and imaginary parts that ($\varepsilon(w)= \varepsilon_1(w)+i\varepsilon_2(w)$) of $\varepsilon(w)$ are

$$\varepsilon_1(w) = 1 - \frac{w_p^2\tau^2}{1 + w^2\tau^2} \tag{2.6}$$

$$\varepsilon_2(w) = \frac{w_p^2 \tau}{w(1 + w^2\tau^2)}$$

This model is known as the Drude model [13]. Optical parameters for silver are; $\gamma\hbar=0.06eV$ and $w\hbar=7.9eV$, for gold; $\gamma\hbar=0.18eV$ and $w\hbar=8.5eV$ [56]. For $w_p<w$, metals sustain their metallic behavior. Large frequencies near w_p, and with $w\tau>>1$, leads to negligible damping, so that $\varepsilon(w)$ becomes dominantly real and dielectric function of the undamped free electron plasma can be expressed as;

$$\varepsilon(w) = 1 - \frac{w_p^2}{w^2} \tag{2.7}$$

The behavior of noble metals in this frequency regime changes with the effect of interband transitions that causes an increase in ε_2. Low frequencies and $w\tau<<1$, results in $\varepsilon_2>>\varepsilon_1$, imaginary part of the dielectric function becomes non-negligible, real and imaginary part of the refractive index become comparable in magnitude with

$$n \approx \kappa = \sqrt{\frac{\varepsilon_2}{2}} \tag{2.8}$$

In this low frequency regime, metals are absorptive.

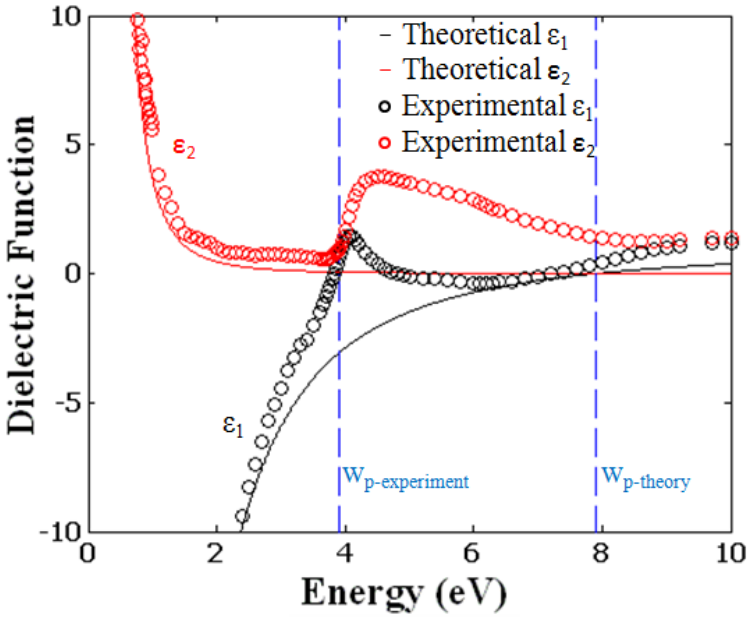

Figure 2.1: Real part, ε_1 and imaginary part, ε_2 for silver calculated from Drude model and experimentally extracted data by Palik [54].

Fig. 2.1 shows the real and imaginary parts of dielectric function for silver calculated using Drude model and compared with experimentally obtained data by Palik [54]. Dielectric function is plotted as a function of the energy. Theoretically calculated ε_1 changes sign from negative to positive beyond the theoretical plasma frequency $w_{p\text{-}theory}$. For energies above $w_{p\text{-}theory}$, metal becomes transparent to the applied electric field i.e. electrons cannot respond to the applied electric field.

Drude model can describe the optical properties of metals for photons that have energies below the threshold of transitions between electronic bands. For some noble metals used in plasmonic applications like silver and gold, interband transitions start occurring around 2 eV [33] and Drude model fails for higher energies.

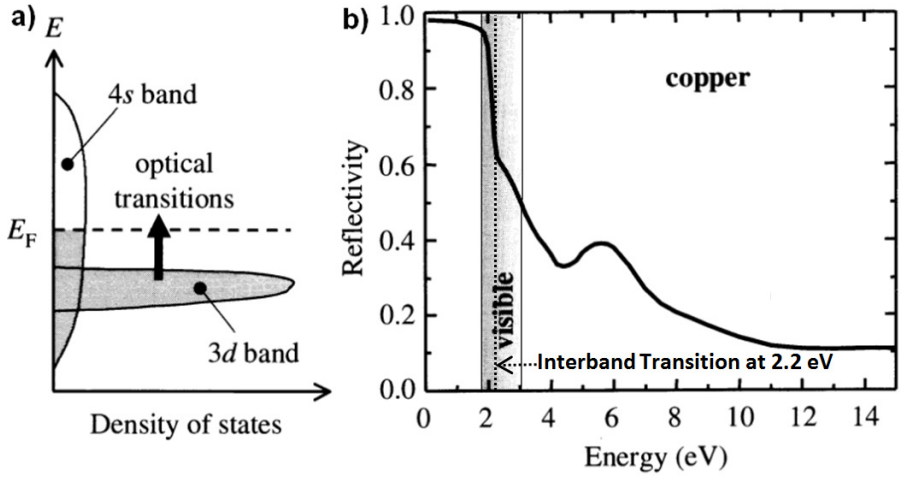

Figure 2.2: a) Schematic density of states for the 3d and 4s bands of a transition for copper. b) Reflectivity of copper. [33].

Interband excitations of electrons modify the dielectric properties of the metals and cause a dramatic drop in the reflection spectrum of the metal which defines the color of the metal in reflection and transmission. For example, copper has an electronic configuration of $[Ar]3d^{10}4s^1$. Fig.2.2 (a) shows the density of states for 3d and 4s orbitals for copper. 4s bands form a broad band that cover a wide range of energies. The narrow 3d bands can keep 10 electrons; therefore density of states is sharply peaked. 4s band can hold 2 electrons and the peak is wider and smaller. The 11 valance electrons fill the 3d orbital and half of the 4s orbital, so that Fermi energy is within the 4s orbital and above the 3d orbital. As a result, interband transitions from filled 3d bands below the Fermi level to unoccupied 4s orbitals above Fermi level is possible. The lowest transition energy is 2.2 eV. Reflectivity drops sharply for energies above 2.2 eV resulting in red color as seen in Fig.2.2 (b) [33]. For silver, electronic configuration is $[Kr]4d^{10}5s^1$ where energies of the 4d and 5s orbitals are close to each other and they are just below the Fermi level, the energy difference between these orbitals is around 3.9 eV. This causes the plasma energy to shift to 3.9 eV. So, interband absorption edge is round 3.9 eV which

results in the reflectivity to remain high throughout the whole visible spectrum. For gold, same phenomenon is valid and interband absorption edge is round 2.6eV which causes the color of gold to be in yellow.

Lorentz modified the Drude model to include absorption at a specific energy [56]. Vial et.al. combined the Lorentz model and Drude model which leads to a modified dielectric function [34] in good agreement of theory with experiment. However, for our purposes in this thesis, Drude model suffices for us to understand the properties of SPPs.

Similar arguments can be constructed through the refractive indices of materials. Complex refractive index n is defined as $\tilde{n}(w)=n(w)+i\kappa(w)$. Refractive index n and absorption coefficient κ can be calculated from the dielectric functions as

$$n = \frac{\varepsilon_1}{2} + \frac{1}{2} + \sqrt{\varepsilon_1^2 + \varepsilon_2^2} \tag{2.9}$$

$$\kappa = \frac{\varepsilon_1}{2n}$$

Fig. 2.3 shows refractive indices and absorption coefficients for silver, calculated from the Drude model and experimentally extracted data by Palik. Refractive index approaches to zero for energies that are close to plasma energy and absorption coefficient also approaches to zero near the plasma energy and metals behave like a dielectric and becomes transparent for higher energies. Such an affect results in a drop in reflection spectrum and part of the spectrum is absorbed. This absorption determines the color of the metal.

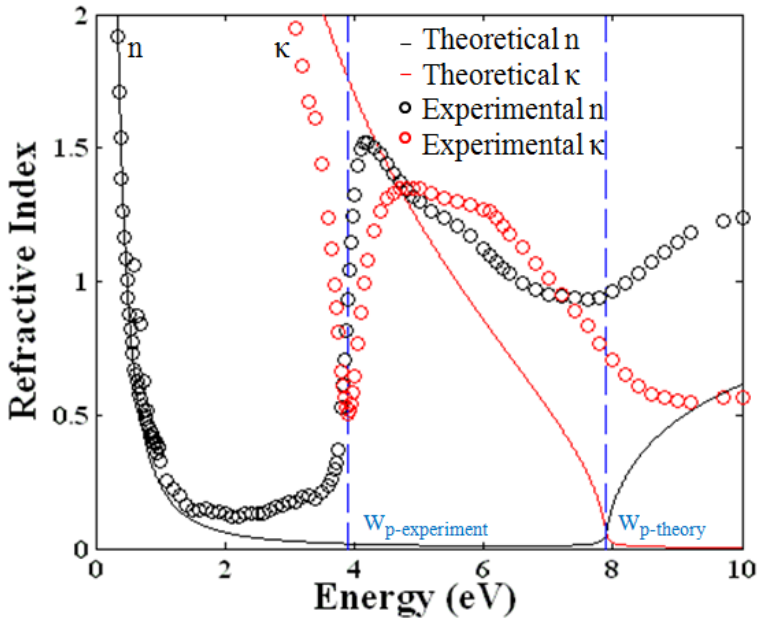

Figure 2.3: Refractive indices, *n* and absorption coefficients, *κ* for silver calculated from Drude model and compared with experimentally extracted data by Palik [54].

2.2. Fundamentals of SPPs

To understand the properties of SPPs one need to calculate the energy-momentum relation (dispersion) of SPPs. SPPs are confined at the metal dielectric interface. Starting with Helmholtz equations at the metal-dielectric interface with constant dielectric permittivity and proper boundary conditions, SPP dispersion relations can be derived. According to the coordinate system in Fig. 2.4, confined wave propagation at the metal-dielectric interface can be defined. Dielectric permittivity is constant in the xy plane and changes at z=0. If z>0, ε_1 is the dielectric permittivity, if z<0, ε_2 is the dielectric permittivity. The wave propagates in the x direction.

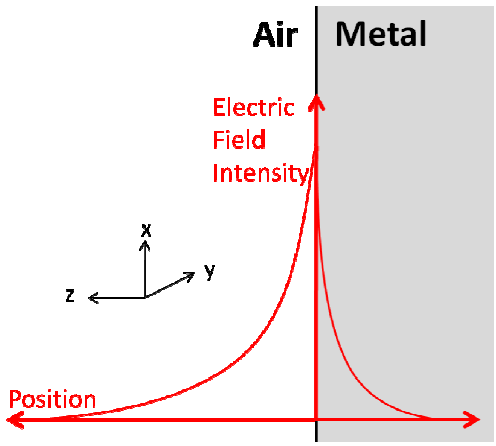

Figure 2.4: Electric field intensity profile of a SPP propagating at the metal dielectric interface.

Starting with the wave equation

$$\nabla^2 E - \frac{\varepsilon}{c^2}\frac{\partial^2 E}{\partial t^2} = 0 \qquad (2.10)$$

and assuming harmonic approximation

$$E(r,t) = E(r)e^{-i\omega t}E(r,t) \qquad (2.11)$$

We reach Helmholtz equation

$$(\nabla^2 + k_0^2\varepsilon)\,(E,H)=0. \qquad (2.12)$$

where k_0 ($k_0=w/c$) is the momentum of light in air. With propagation along the x axis and for TM modes we can assume

$$E(r,t)=E(z)e^{i\beta x} \qquad (2.13)$$

$$H(r,t)=H(y)e^{i\beta x}$$

where β is the propagation constant along the x direction. Inserting Eq. 2.1 into 2.2 results in

$$\frac{\partial^2 E(z)}{\partial z^2} + (k_0\varepsilon - \beta^2)E(z) = 0 \qquad (2.14)$$

$$\frac{\partial^2 H(y)}{\partial y^2} + (k_0\varepsilon - \beta^2)H(y) = 0$$

The field components at z>0 can be defined as

$$H_y(z) = A_2 e^{i\beta x} e^{-k_2 z}, \qquad (2.15)$$

$$E_x(z) = iA_2 \frac{1}{w\varepsilon_0\varepsilon_2} k_2 e^{i\beta x} e^{-k_2 z},$$

$$E_z(z) = -A_2 \frac{\beta}{w\varepsilon_0\varepsilon_2} k_2 e^{i\beta x} e^{-k_2 z}.$$

The field components at z<0 can be defined as

$$H_y(z) = A_1 e^{i\beta x} e^{-k_1 z}, \qquad (2.16)$$

$$E_x(z) = iA_1 \frac{1}{w\varepsilon_0\varepsilon_1} k_1 e^{i\beta x} e^{-k_1 z},$$

$$E_z(z) = -A_1 \frac{\beta}{w\varepsilon_0\varepsilon_1} k_1 e^{i\beta x} e^{-k_1 z}$$

where k_1 and k_2 are positive. Continuity at boundary conditions at z=0 results

$$A_1 = A_2 \qquad (2.17)$$

$$\frac{k_2}{k_1} = -\frac{\varepsilon_2}{\varepsilon_1}$$

$$k_1^2 = \beta^2 - k_0^2 \varepsilon_1^2$$

$$k_2^2 = \beta^2 - k_0^2 \varepsilon_2^2$$

These equations are satisfied if and only if ε_1 and ε_2 has opposite signs. At metal dielectric interfaces, this condition is satisfied at a specific frequency interval from

zero to plasma frequency. If we solve these equations, we get the dispersion relation for SPPs as

$$k_{SPP} = \frac{w}{c}\sqrt{\frac{\varepsilon_1\varepsilon_2}{\varepsilon_1+\varepsilon_2}} \tag{2.18}$$

where $\beta=k_{SPP}$ and $k_0=w/c$. k_{SPP} is always larger than k_0, which implies that photons in free space cannot directly excite SPPs. This condition is known as the momentum mismatch. Dielectric permittivity is constant over a wide range of wavelengths for dielectrics compared with metals and dielectric permittivity of metals changes very dramatically for visible wavelengths. A singularity is obtained when $\varepsilon_{1=}\text{-}\varepsilon_2$. From the Drude model, this singularity is calculated as

$$w_{SP} = \frac{w_p}{\sqrt{1+\varepsilon_2}} \tag{2.19}$$

This frequency is known as the surface plasmon resonance frequency. Contribution of the d orbital electrons in silver causes this frequency to shift to 3.7 eV [13].

Fig. 2.5 represents the dispersion relation for silver-air interface. SPPs bound to the interface can be identified as the curve below the light line up to surface plasmon resonance frequency at 3.7 eV. Bound plasmons are SPPs confined at the metal dielectric interface propagating along the interface. In the SPP bound mode regime, momentum of light in air is less than the momentum of SPP for the same energies. Because, SPPs are collective oscillations of free electrons and photons, SPPs can be visualized to have both electron and photon parts where momentum of electrons are larger than the momentum of light with the same energy. This phenomenon causes the momentum miss match. The difference in momentum prevents the SPP excitation with incident light in air. There are several methods to compensate for the momentum miss match which will be discussed later.

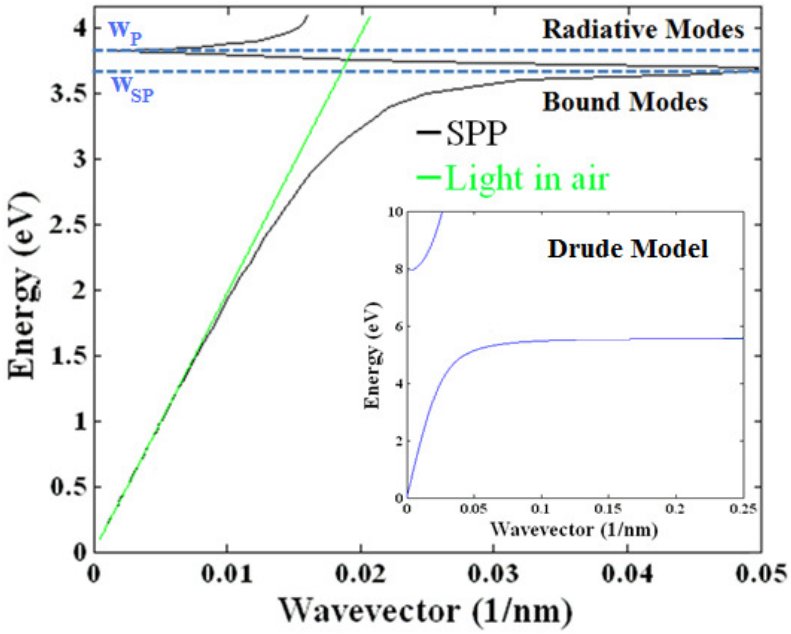

Figure 2.5: Surface plasmon polariton dispersion relation for silver-air interface and dispersion of light in air. Dispersion of SPP is calculated with the Drude model as represented in the inset [13].

Radiative modes are energetic SPPs that are above the w_p (3.9 eV) which are above the light line. In this regime, radiative bulk plasmon modes are observed and the metal behaves like a dielectric and dielectric function of the metal is larger than positive. Light with large wave vectors can excite characteristic surface plasmon frequencies w_{sp} around 3.7 eV. Between 3.7 eV and 3.9 eV region, plasmonic modes are called quasi-bound modes where SPPs exhibit negative phase velocity. In this regime, according to Drude model, dispersion is purely imaginary and SPPs are not allowed to propagate and this imaginary region behaves like a band gap, but, experimentally these modes can be excited.

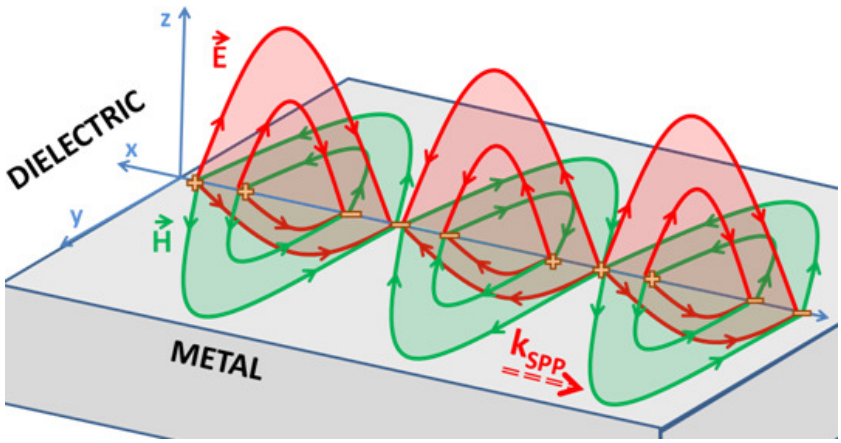

Figure 2.6: Electric and magnetic field distributions of SPPs propagating at the metal-dielectric interface.

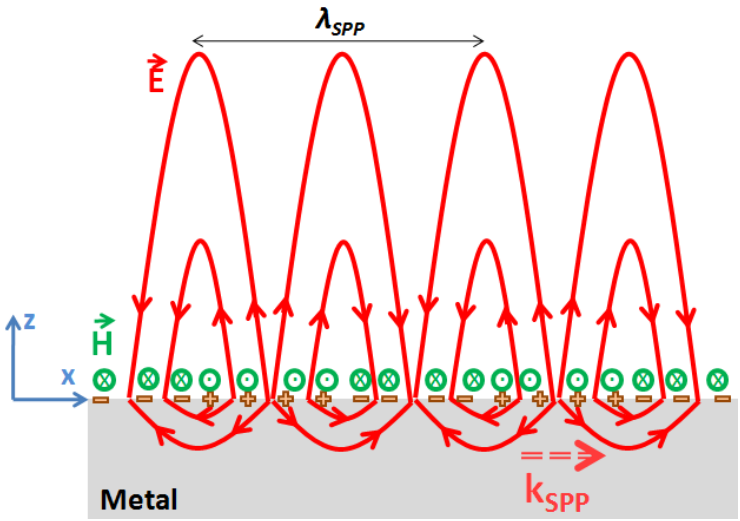

Figure 2.7: Cross section view from the x-z plane, of electric and magnetic field distributions of SPP propagation at the metal-dielectric interface.

Electric and magnetic field distribution of SPP propagation at metal dielectric interfaces for TM (TM represents transverse magnetic and in TM mode, there is no magnetic field in the direction of propagation) polarization is shown in Fig. 2.5 and Fig. 2.6. Electric fields are created by positive and negative charges on surface of the metal. H field has only the component parallel to the interface. E field has both

parallel and perpendicular field lines with respect to the interface. E field's perpendicular components in the two media are in opposite directions and E field's parallel components in the two media are in the same direction. The boundary conditions are the continuity of $E_{//}$ ($E_{//}$ is the parallel component of E) and $D_{\perp}$ ($D_{\perp}$ is the perpendicular component of D and $D=\varepsilon E$). The continuity of $D_{\perp}$ is satisfied for positive values of ε_1 and negative values of ε_2 a condition that is only satisfied for metal-dielectric interfaces and as a result, surface plasmons exists only at the metal-dielectric interfaces. H fields should be divergence free which indicates absence of magnetic monopoles. This means that the end points of the H field lines should be in the same direction. For a TE (TE represents transverse electric and in TE mode there is no electric field in the direction of propagation) polarized solutions, boundary condition for the continuity of $H_{//}$ is violated because the H field directions are in opposite directions at the metal dielectric interface and TE polarized SPPs cannot be excited at the metal dielectric interfaces [35].

The wavelength of the SPPs is the period of the charge distribution on the surface and the associated field distributions. Real part of dispersion relation describes the wavelength of SPP and imaginary part of dispersion relation describes the loss or the propagation length of SPPs. Real part of the SPP dispersion is

$$k_{SPP-real} = k_0 \sqrt{\frac{\varepsilon_d \varepsilon_{m1}}{\varepsilon_d + \varepsilon_{m1}}} \tag{2.20}$$

where ε_{m1} is the real part of dielectric function for the metal and ε_d is the dielectric function of dielectric. SPP wavelength can be written as

$$\lambda_{SPP}=2\pi/k_{SPP\text{-}real} \tag{2.21}$$

$$\lambda_{SPP} = \lambda_0 \sqrt{\frac{\varepsilon_d + \varepsilon_{m1}}{\varepsilon_d \varepsilon_{m1}}}$$

Wavelength of the SPPs is smaller than the wavelength of photon in air which allows us to study optics below the diffraction limit i.e. called sub-wavelength optics. Wavelength of light in air can be reduced to 4-5 times smaller wavelengths by exciting SPPs with energetic photons around 3.6-3.7 eV at the silver- air interface [54].

SPPs cannot be excited with light without overcoming momentum mismatch between light in air and SPP. Methods like prism coupling or grating coupling to excite SPPs are necessary to compensate the momentum mismatch [12]. There are also other methods like the use of trench scatterers, charged particle impact and near field coupling [35]. Prism coupling and grating coupling is the most common ways to excite SPPs.

In grating coupler method, grating surfaces can compensate the missing momentum with additional momentum to the incident light caused by the periodicity of the grating. Grating coupler allows to excite SPPs when light is incident from above the grating or below the grating. According to Fig. 2.8 (a), SPPs can be excited using grating coupler with the condition

$$k_{spp} = k_0 \sin(\theta) \pm mG \qquad (2.22)$$

where G ($G = 2\pi/a$) is the reciprocal lattice vector of the grating and m is the order of diffraction. By changing the incidence angle and wavelength of light and measuring the reflected intensity, SPP modes supported by the surface can be detected.

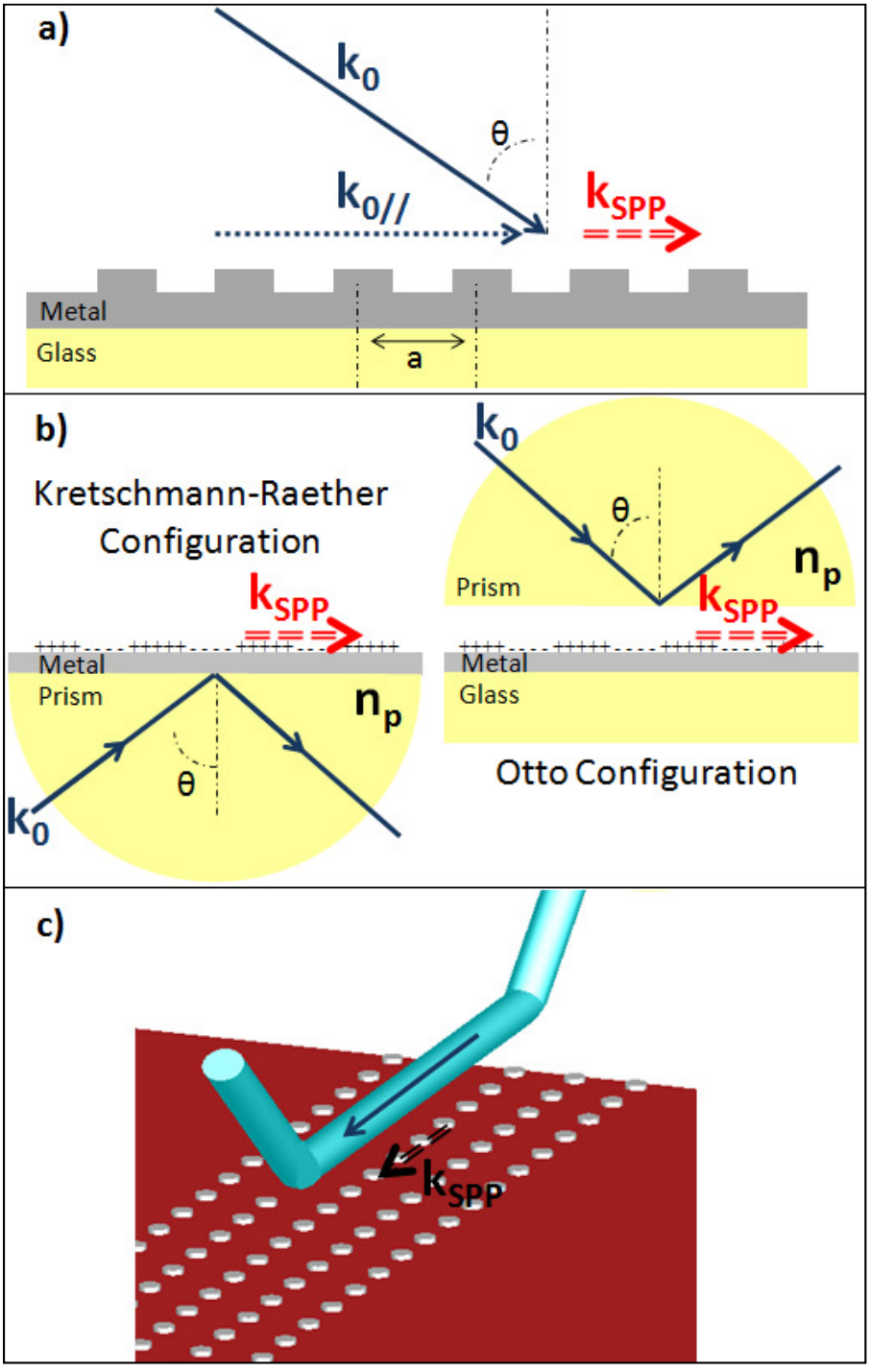

Figure 2.8: Schematic representations of (a) grating coupler and (b) prism coupler (c) near field fiber coupler.

High refractive index prisms can enhance the momentum of incident light by a factor determined by the refractive index of the prism, n_p. According to Fig. 2.8 (b) (Kretschmann-Raether configuration and Otto configurations are shown respectively), when the parallel component of the momentum of the incoming light in the prism is equal to the momentum of SPP and energy of the incident photon is equal to energy of SPP, SPPs can be excited. The momentum matching condition is given by

$$k_{spp}=n_p k_0 sin(\theta) \tag{2.23}$$

where k_{spp} is the momentum of SPP, n_p is the refractive index of the prism, k_0 is the momentum of incident light and θ is the incidence angle. SPP modes can be measured by scanning the incidence angle or wavelength of light and measure the reflected intensity. Incident light penetrates into the metal-air interface to excite the SPPs and part of the light reflects back from prism-metal interface. SPPs reradiates back to the prism resulting in destructive interference between the radiated light from the SPPs and light reflected back from prism-metal interface. If the reflected intensity becomes minimum, this indicates that an SPP is excited. Fig. 2.9 schematically describes the momentum mismatch. Consider for the same energies of SPP at metal-air interface with momentum k_2, light in air with momentum k_1 and light in prism with momentum k_3. Momentum of light in air is less than momentum of the SPP; momentum of light in prism is higher than the momentum of SPP. As the momentum of the SPP has only parallel component to the surface with momenta k_2, this component of the light incident through the prism at an angle to the prism-metal interface can be tuned to become less than k_3 by changing the angle of incidence, and matching k_2. When this parallel component is equal to k_2, SPP is excited by the incident light with momentum matched.

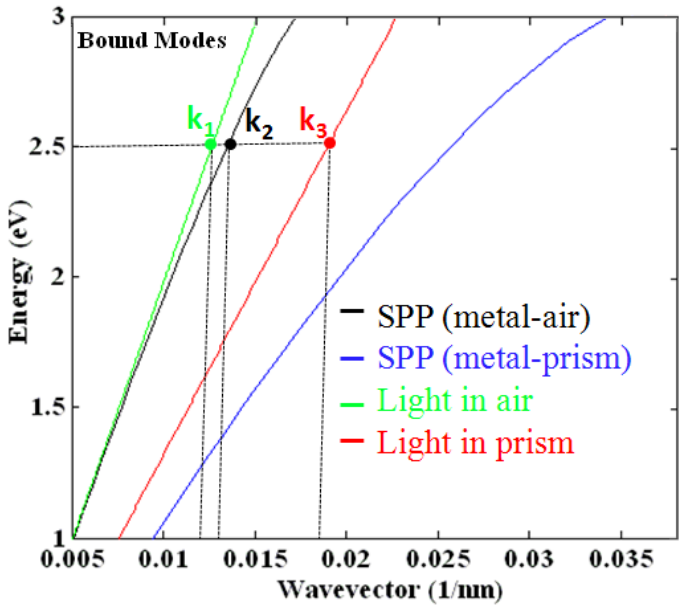

Figure 2.9: Illustration of momentum mismatch between the surface plasmon polariton and light superimposed on the long wavelength part of the dispersion curve.

Another method to excite SPPs that is suitable for integrated optics applications is the use of a fiber coupler. Fig. 2.8 (c) represents the fiber coupler. A fiber can be mobile on two dimensional metal nanoparticle plasmon waveguide structures for evanescent phase-matched coupling. Excitation condition is satisfied as momentum and energy are matched when fiber is in close proximity of the plasmonic structure. This condition is satisfied only when the dispersion curve for the photonic modes of the fiber and the SPPs at the metal-air interface cross at a particular momentum. Waveguide structures can be designed to support SPP modes for such an excitation. High coupling efficiency of %75 can be achieved by this method [36].

2.3. Propagation of SPPs on Periodic Surface

An analogy with solid state physics and photonic crystals can be constructed to understand the dispersion relation of the SPPs in periodic medium. In solid state physics, electrons in a crystal can be considered to be in a periodic potential due to periodicity of the atoms. Electrons are not allowed to have all momentum and energy because of the periodic potential. The ranges of energies that cannot be occupied by electrons are called the forbidden band or the electronic band gap. In the case of photonic crystals, periodic structure consisting of two materials with refractive indexes of n_1 and n_2 as seen in Fig. 2.10 (a) can also generate a photonic band gap, provided that the Bragg condition is satisfied

$$k_{SPP}=G/2 \tag{2.24}$$

where G is reciprocal lattice vector. Bragg scattering of light results in both forward and backward traveling waves and interfere constructively results in a standing wave [17]. Light at each interface interfering constructively in the plasmonic structure forms two standing wave profiles with different energies. The maxima of the high energy (ω^+) standing wave form in the lower index material and the maxima of the low energy (ω^-) standing wave occur in the high index material. For energies between ω^- and ω^+ light interfere destructively and light propagation is not allowed. Hence, a band gap is formed, known as the photonic band gap. Electric field distributions at the edges of the band gap are shown for the photonic case in Fig. 2.10 (a). The formation of the band gap for the plasmonic case has an analogy with the photonic case.

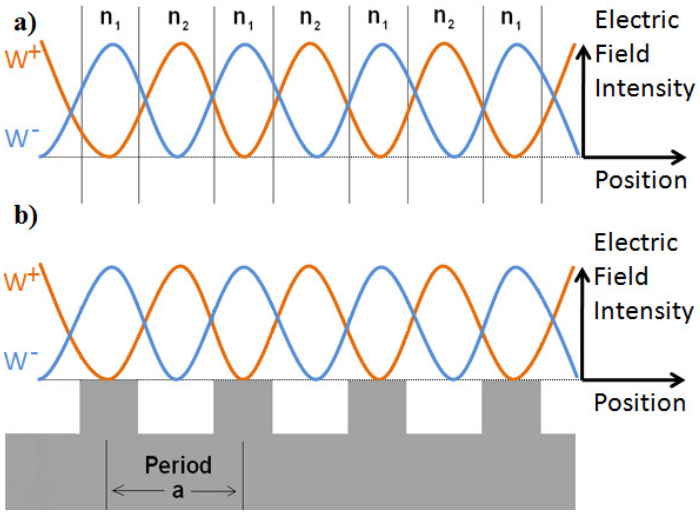

Figure 2.10: Standing wave profiles of a) light in photonic crystal, and b) SPP on the periodic surface.

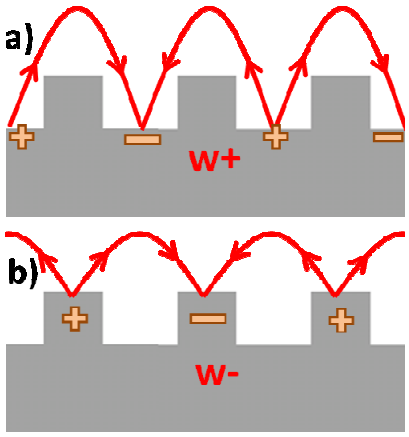

Figure 2.11: Electric field distributions for a) ω^+ and b) ω^- modes.

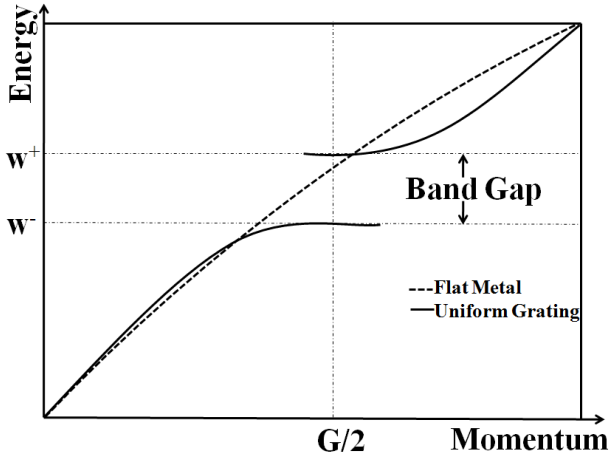

Figure 2.12: Schematic representation of dispersion relation of SPPs for the uniform metallic grating and flat metal.

For SPPs, corrugations on the grating surface act as scattering centers and effective index of the plasmon changes periodically as it travels along the grating. The periodicity of the grating causes scattering of SPPs and when the Bragg condition in Eq. 2.15 is satisfied, a band gap develops at the corresponding energy at a specific momentum. It is possible to excite SPPs with the same momentum but with different energies. Two different electric field distributions at the band edges with different energies are shown in Fig. 2.11. For higher energy configuration in figure 2.11(a), charges and electric field are located on the troughs. For lower energy configuration in figure 2.11(b), charges and electric field are localized on the peaks of the grating. This behavior is very similar to photonic case.

Dispersion relation of SPPs for the metallic grating is shown in Fig. 2.12. A band gap is formed at the momentum where Bragg condition is satisfied and two plasmonic states with different energies are formed with the same momentum. Two plasmonic states with energies ω^+ and ω^- are standing waves and the slope of the dispersion line describes the group velocity of the wave

$$v_g = d\omega/dk \qquad (2.25)$$

2.4. Localization of SPPs

Optical cavities that localize light in the forbidden band gap can be obtained by breaking the symmetry of a photonic crystal [27]. High transmission bands at frequencies within the band gap of the unperturbed photonic crystal can be created [28]. New electromagnetic modes in the cavities are created due to the constructive interference of the photons for wavelengths within the cavity region.

Cavity states can also be created for plasmonic structures by breaking the symmetry of the plasmonic crystal. In the case of metallic gratings, a phase shift element may be introduced into the periodic structure which provides the phase shift upon reflection for SPPs propagating in the cavity. Corrugations on both sides of the phase shift element may be considered to act as a mirror. Such Sampled Bragg mirrors (SBM) can localize SPPs due to phase shift upon reflection [29]. In Fig 2.13 we show a SBM cavity structure that is achieved by adding a phase shift element for every ten ridges to the periodicity of the metallic ridges on a thin film on glass substrate, as shown in Fig. 2.13. For an isolated cavity, the cavity state is dispersionless. For cavities that are in close proximity of each other, SPP modes can couple to each other. Coupling of such cavities have been studied using tight binding approximation which display dispersion. The schematic representation of dispersion for localized SPPs is shown in Fig. 2.14. When such cavities are next to each other and coupled, the dispersion obtained from the tight binding approximation is;

$$\omega(k) = \alpha\,[\,1 + \beta\cos(kD)] \tag{2.26}$$

where D, α, β, k are superperiodicity (cavity to cavity distance) of the cavities, resonance frequency of individual cavity, coupling factor and momentum of SPP respectively [37].

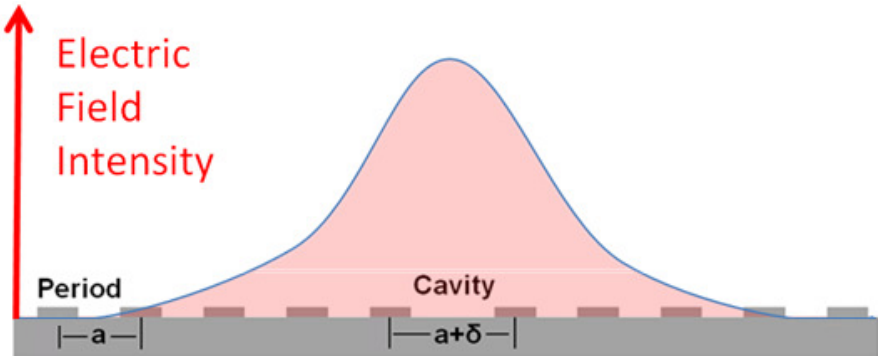

Figure 2.13: Envelope of electric field intensity distribution of SPP excited in a localized cavity state on a SBM, with phase shift of π.

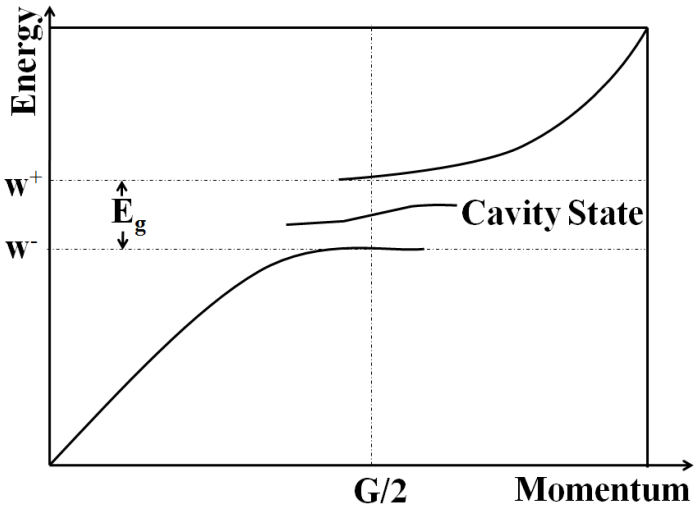

Figure 2.14: Dispersion relation of SPPs for the metallic gratings with a cavity. Note the cavity state in the band gap.

The cavity structure is shown in Fig. 2.13; a phase shift of δ is added to the period to form the cavity. The resonance condition is defined by

$$\delta=(2n+1)\,(\lambda_{SPP}/4) \qquad (2.27)$$

where n is an positive integer starting from zero and defining the number of electric field maximas within the cavity region. The resonance in such a cavity occurs if the

field of the SPP undergoes an integer number of 2π phase shifts after a round trip in the cavity [29,30] (phase shift of π represents the half of the period, 2π represents the period). The resonance SPP electric field distribution is shown in Fig. 2.13. It is possible to excite different electromagnetic modes within the cavity region by changing the phase in SBMs.

There are other types of surfaces that can be used to localize SPPs. Moiré surface is a one dimensional biharmonic grating that has a superperiod obtained by adding two periodicities that are close to each other. Moiré surfaces can also localize SPPs due to a phase shift of π at every node [31]. Alternatively, one can create a cavity on a biharmonic grating by selectively dielectric coating the metallic surface which causes periodic changes in the effective index of SPPs. This index variation can control the phase properties of SPPs and enable plasmonic cavity modes [32].

2.5. Simulation of SPP propagation in Plasmonic Structures

In order to gain further insight to the physics of SPP formation, propagation and localization, we can numerically solve the paraxial wave equation. This can be achieved by several techniques. Finite difference time domain (FDTD) is a powerful technique for solving Maxwell's equations with boundary conditions. The formulation of this iterative method was described by Yee as follows [38]:

The plasmonic structure is placed in a computation window chosen suitably as larger than the structure under consideration. The computation window (and the plasmonic structure) is then divided by a three dimensional grid each of which is called the Yee cell. The distance between grid points, Δx, Δy, Δz, are chosen to be

small enough that they do not change significantly in from one to the next. For a stable solution, the condition that

$$\sqrt{(\Delta x)^2 + (\Delta y)^2 + (\Delta z)^2} > c\Delta t = \sqrt{\frac{1}{\epsilon\mu}} \times \Delta t \qquad (2.28)$$

must be met. In a two dimensional system in which we have a homogeneous medium along one axis (z-axis), ϵ and μ is constant along z axis and J=0, then the electromagnetic fields for transverse magnetic (TM) can be expressed in difference form as

$$E_z^{n+1}(i,j) = E_z^n(i,j) + Z\frac{\Delta\tau}{\Delta x}\left[H_y^{n+1/2}(i+1/2,j) - H_y^{n+1/2}(i-1/2,j)\right] \qquad (2.29)$$

$$-Z\frac{\Delta\tau}{\Delta y}\left[H_x^{n+1/2}(i,j+1/2) - H_x^{n+1/2}(i,j-1/2)\right]$$

$$H_x^{n+1/2}(i,j+1/2) = H_x^{n-1/2}(i,j+1/2) + \frac{1}{Z}\frac{\Delta\tau}{\Delta y}[E_z^n(i,j+1) - E_z^n(i,j)]$$

$$H_y^{n+1/2}(i+1/2,j) = H_y^{n-1/2}(i+1/2,j) + \frac{1}{Z}\frac{\Delta\tau}{\Delta x}[E_z^n(i+1,j) - E_z^n(i,j)]$$

where $Z=(\mu/\varepsilon)^{1/}2$, $\Delta\tau=c\Delta t$ (c is the speed of light, t is the time), n is the time iteration, i is the vector component on x-axis and j is the vector component on y-axis. These equations are solved iteratively for given initial conditions. To start the simulation, we can launch two different types of waves into the plasmonic structure. They are incident waves such as a plasmonic mode on the metal-air interface or a plane wave incident on the prism-metal interface.

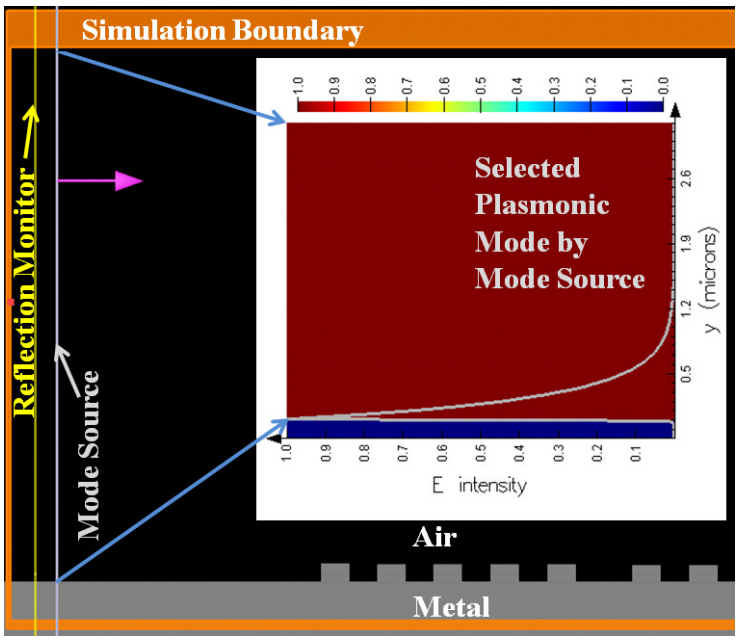

Figure 2.15: Simulation window for SPP mode source configuration using Lumerical software. Inset: Electric field intensity distribution of a plasmonic mode at the metal-air interface calculated by the source.

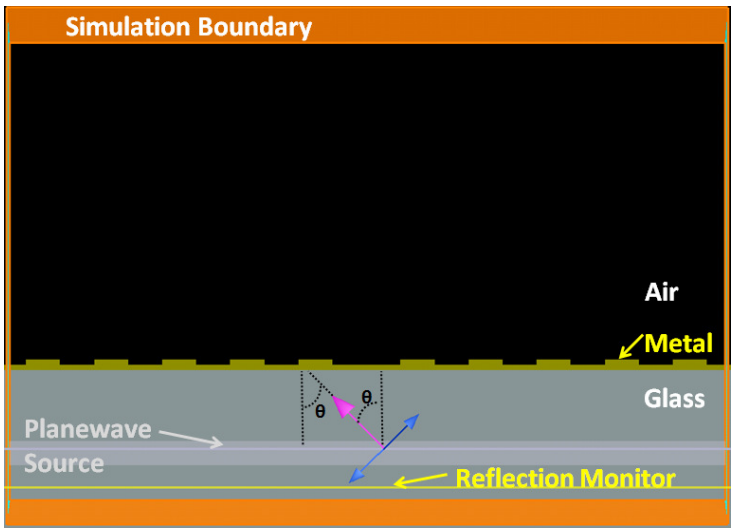

Figure 2.16: Simulation window for plane wave source configuration used to calculate the dispersion relation of the plasmonic structure.

Demonstration version of the commercially available Lumerical software (Lumerical Solutions, Vancouver, Canada) is used for the FDTD simulations [55]. Two methods are used to simulate the plasmonic structures. First method is the SPP mode source configuration method. We can select the plasmonic mode electric field distribution to launch SPPs at the metal-dielectric interface. The method is defined as follows: first, define a physical structure, select simulation parameters and position of light source and monitor. Second, choose plasmonic mode at the metal-dielectric interface for the selected wavelength interval which lets to launch electric field intensity distribution for SPPs in two dimensions. Third, run the simulation and measure reflection intensity scattered back from the interface using the monitor. A sample simulation set up is shown in figure 2.15. SPP mode propagates at the interface between the metal and air. A light source is positioned between the grating structure and the reflection monitor. Reflection monitor records the back reflected light intensity. SPP modes supported by the plasmonic structure are measured by this method. This simulation set up does not give information about the momentum-energy relation of SPP modes supported by the system; it only gives the information about the energy of the SPPs supported by the plasmonic structure.

Second method is the plane wave source configuration, which is defined as follows: First, define the physical structure and select simulation parameters and position of light source and monitor. Second, choose a wavelength and angle of incidence for the source. Third, run the simulation and measure reflection intensity scattered back from the interface using the monitor. Fourth, repeat the second step and the third step for the desired incidence angle and wavelength intervals with the help of a script file. A light source is positioned between the grating structure and the reflection monitor as shown in Fig. 2.16. Plane wave propagates in glass and reflects from the metal surface and exciting SPPs. Reflection monitor records the back reflected light intensity as a function of wavelength and incidence angle. This simulation set up gives information on the dispersion of SPPs.

Chapter 3

3. Fabrication and Characterization of Plasmonic Structures

In this chapter, we discuss fabrication of SPP structures using electron beam lithography. Polarization dependent optical characterization of SPP structures has been achieved using an ellipsometer configured as reflectometer. Furthermore, we give details of instrumentation of optical measurements system using reflectometer.

3.1. Fabrication of SPP Cavities Using Electron Beam Lithography

Electron beam lithography (EBL) is a method to define a pattern on the surface of a thin film sensitive to electron impact called the electron beam resist. For many applications, the positive photoresist, poly methyl methacrylate (PMMA) is used as the electron beam sensitive film [39]. Simply described, an electron beam exposes selected areas of the resist and a developer removes the exposed areas of the

positive resists. In the case of negative resists, areas that are not exposed are removed after developing the resist. The aim is to write very small features into the resist which can be transferred to the substrate material placed under the PMMA film.

The biggest advantage of electron beam lithography is its ability to create features below the diffraction limit of light i.e. features at the nanometer scale; this is possible due to the small spot size and the short wavelength of the electrons. Electron beam lithography is a maskless process and it can also be used to create photomasks which are used in photolithography.

One of the limitations of electron beam lithography is the long exposure times for a large area substrate. During long exposure times, beam may drift or electron current from the source may become unstable. [40]

A scanning electron microscope (SEM, CamScan CS3200) was modified with a laser interferometric stage (Softsim) and a pattern generator system (Xenos) to be used as an electron beam lithography system [41]. The procedure to create metallic gratings on a thin glass substrate is as follow:

- Glass substrate is washed with de-ionized water (DI).
- 35 nm of silver is evaporated onto the glass slide in a thermal evaporator.
- PMMA A4 495 is spun onto the sample for 5 seconds at 400 rpm and then at 3000 rpm for 40 seconds resulting in a thickness of about 190 nm [42].
- Sample is soft baked in a convection oven at 170° C for 5 minutes.

- PMMA A2 950 is spun onto the sample for 5 seconds at 400 rpm and then 3000 rpm for 40 seconds that results in a thickness of about 60 nm. This bi-layer structure is used to achieve the desired undercut for lift-off.
- Sample is soft baked in convection oven at 170° C for 20 minutes.
- 1 nanocoulomb line dose is exposed at 15kV on the sample to form line gratings (Dose = dwell time x electron current).
- Sample is developed in 1:2 MIBK:IPA (Methyl Isobutyl Ketone:Isopropyl Alcohol) for 70 seconds.
- Sample is placed in isopropyl alcohol for 60 seconds.
- Sample is washed with DI water for 60 seconds.
- Sample is checked under the microscope and if necessary, sample is developed for a longer time.
- 25 nm of silver is evaporated in the thermal evaporator.
- Sample is placed in hot acetone (70° C) and washed in acetone with the help of a glass hypo to force acetone flow on to the PMMA until all metal is lifted.
- Sample is placed in an ultrasonic bath while it is still in acetone for 5 seconds.
- Sample is taken out and washed with isopropyl alcohol and then washed with DI water.
- Sample is checked under the microscope for the lift off achievement.
- Sample is checked for the line widths and periods and defects under the SEM. Samples with very low defects are selected for measurement.

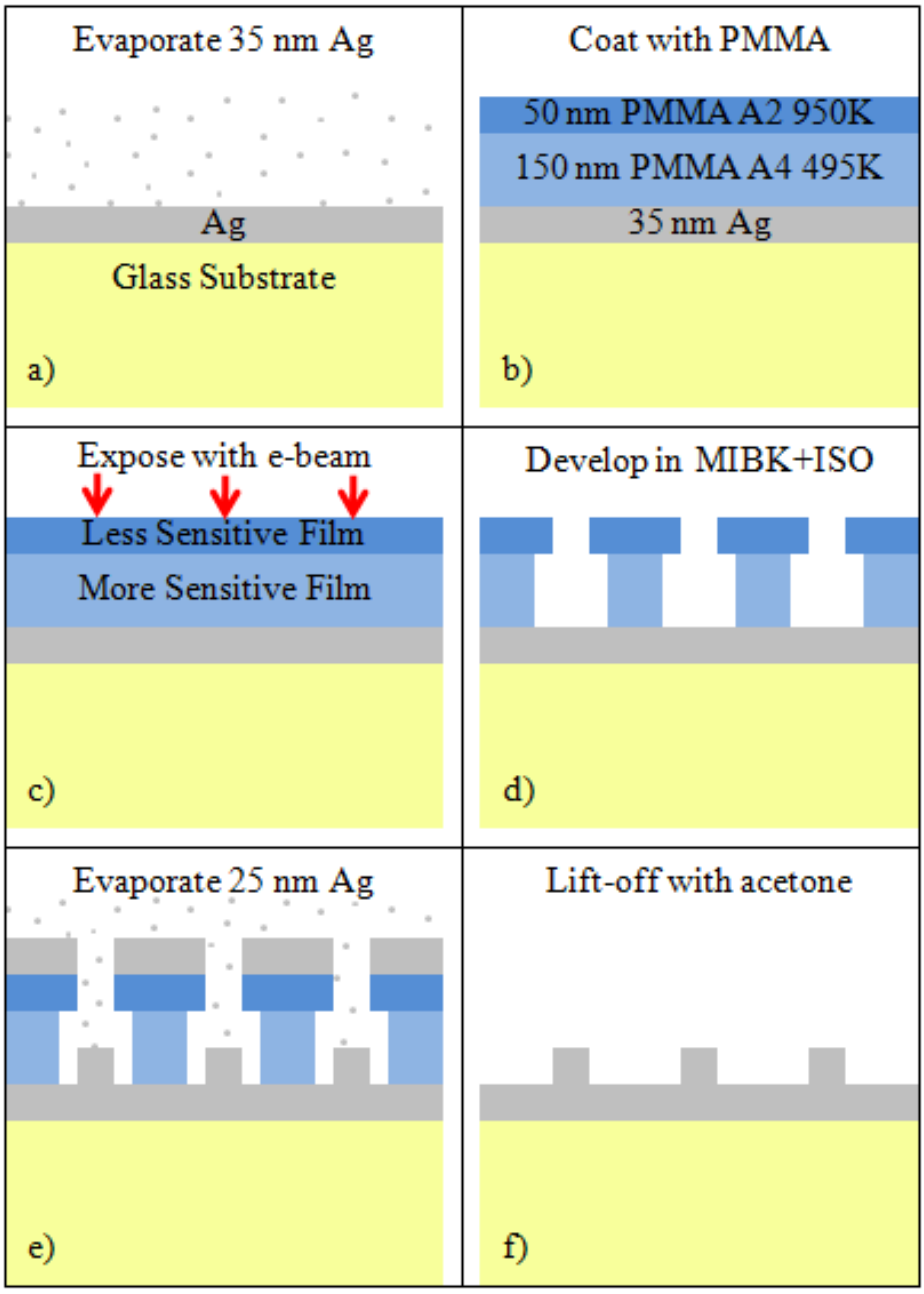

Figure 3.1: Schematic representation of bi-layer undercut process.

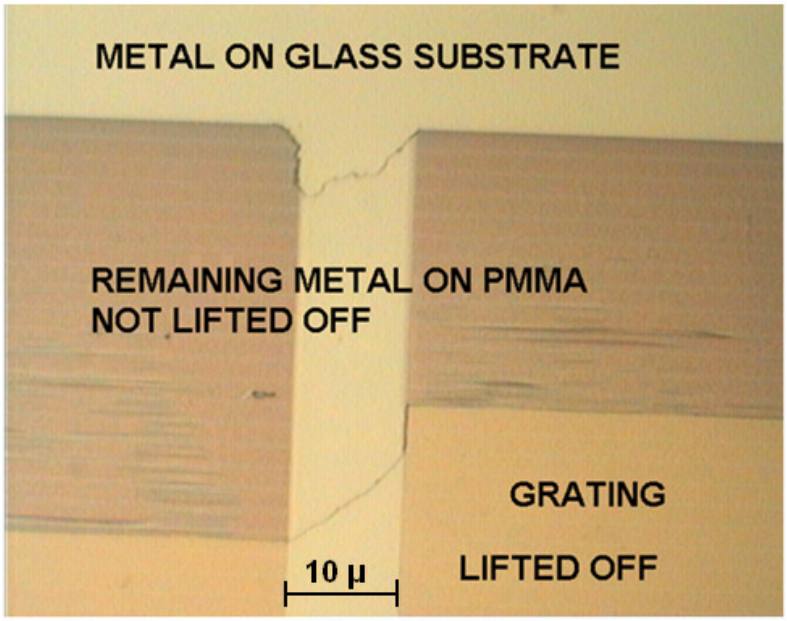

Figure 3.2: A photograph of a sample taken by the optical microscope which is partially lifted off.

PMMA is a positive e-beam resist generally used to create small features at the nano scale. It can be found in two molecular weights of 495K or 950K that is dissolved in chlorobenzene or anisole. 2% 950K (Kilodalton) PMMA in anisole (A2) and 4% 495K PMMA in anisole (A4) is used for bi-layer process undercut. Electron beam exposure breaks down the polymer into smaller fragments that can be dissolved in a 1:2 MIBK:IPA developer. 495K PMMA is more sensitive to electrons so that it is etched more than the 950K PMMA to form an undercut profile. Schematic representation of bi-layer undercut process is shown in Fig. 3.1. Before using bi-layer method, where 100 nm thick single layers of 950K chlorobenzene 2% was used and lift off was a big problem for many samples. With the help of the bi-layer process, this problem was solved and probability of producing gratings increased dramatically.

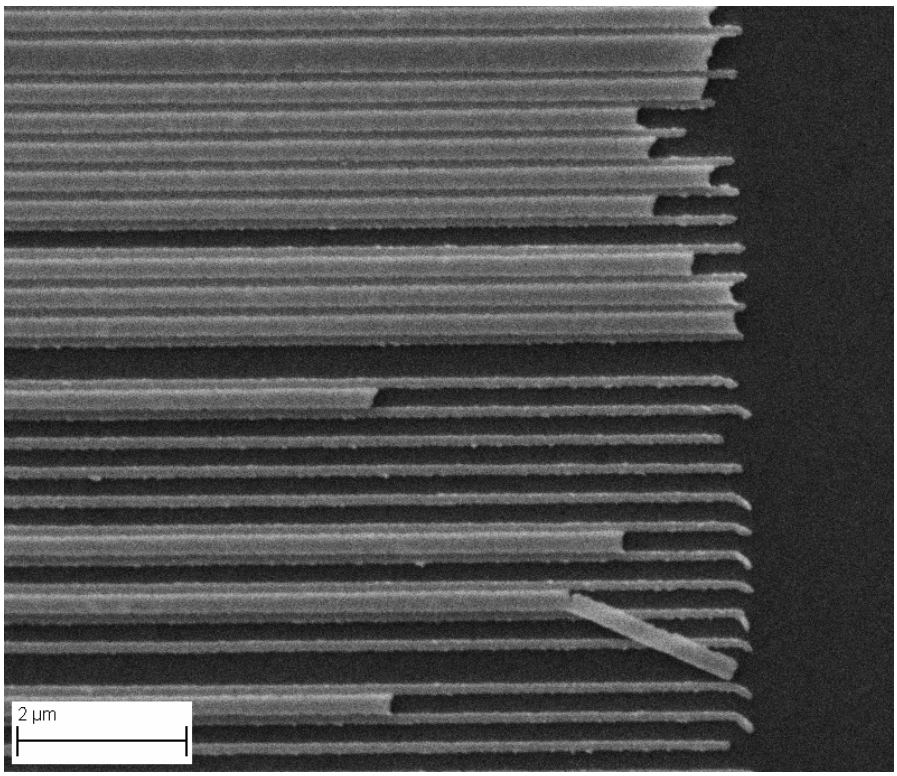

Figure 3.3: SEM image of a SBM that has partially lifted off parts.

The process quality can be checked by an optical microscope or a scanning electron microscope (SEM). Lift off was the major problem in the fabrication of samples, initially. Exposure and development optimization is essential since they effect line width of ridges and the etch profile, where we coat silver. The areas in between the ridges are also critical for the lift of process. If line width of the ridges are narrow and the area in between the ridges are wide (say 300 nm or longer), then the area in between the ridges are hard to break off and parts of the metal still remains on the grating structure. Fig. 3.2 shows a microscope image of a SBM that has remaining metal parts and lifted off parts after liftoff process and Fig. 3.3 shows a SEM image of a SBM that has remaining metal parts after liftoff. An ultrasonic bath for about 10 seconds may sometimes help if a small amount of metal still remains on the grating.

3.1.1. Fabrication of Uniform Gratings

Creating a uniform grating by EBL is achieved by exposing the PMMA covered sample by scanning the surface with electron beam. The line width of the exposed regions depends on the following parameters:

- dose exposed per unit length,
- develop time,
- developer concentration,
- film thickness of PMAA,
- baking time and temperature,
- period of the grating (proximity affect),
- type of PMMA,
- silver thickness under PMMA,
- type of substrate.

The exposed dose on the resist is varied and other parameters listed above are kept the same. Different fields are exposed with different doses. All fields exposed with different doses are processed to the end. This procedure is called the "dose matrix". After checking the dose matrix with SEM, best exposure doses are selected to create gratings for measurements. Then, to fabricate the sample to be measured the chosen dose is used to expose the resist for a total area of 1.5 mm^2. This is done by exposing single 100 μm^2 areas one by one with 5 μm separations in between every field. Matrixes of 14 x 14 (total 196) fields are exposed for the samples that are for measurements. All fields should be successfully fabricated as in Fig. 3.4 for a total area of 1.5 mm^2.

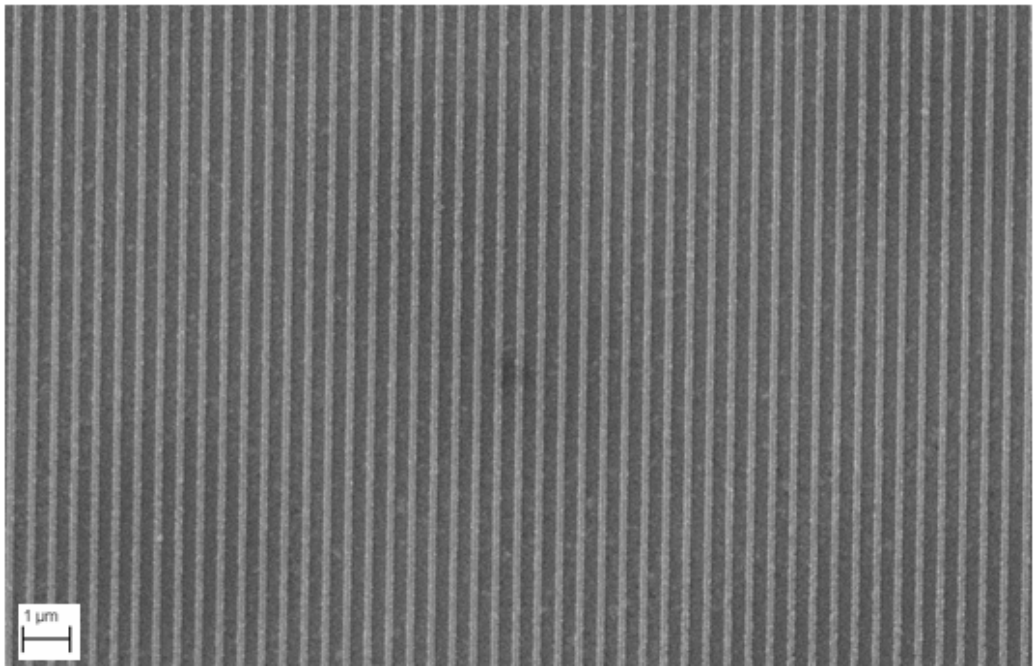

Figure 3.4: Top view SEM image of a uniform grating fabricated by e-beam lithography with a period of 440 nm.

3.1.2. Fabrication of Phase Shifted Gratings

Creating SBM by EBL is achieved by exposing PMMA with single line scans of the electron beam onto the PMMA by adding half of the period in between the lines for every ten lines. This results in a periodic phase shift on the grating. A sample of SBM is shown in Fig. 3.5. All processes are the same for EBL process of fabrication of grating.

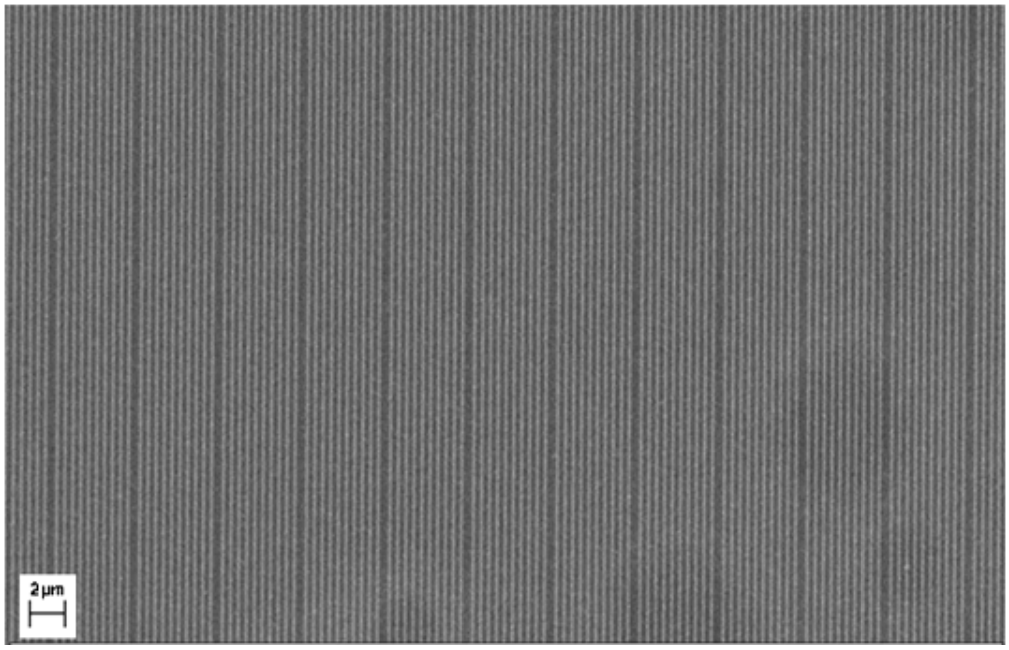

Figure 3.5: Top view SEM image of a SBM fabricated by e-beam lithography with a period of 440 nm.

3.2. Optical Characterization of SPP Structures Using a Reflectometer

An ellipsometer measures the change in polarization of incident light upon reflection or transmission and it is used as an optical technique for the characterization of thin optical films. During this study, we used it as a reflectometer in order to characterize the fabricated SPP cavities. Fig. 3.6 represents the schematic view of the ellipsometer that is used to characterize plasmonic structures. Prism coupler is used to excite SPPs. Index matching fluid is used to prevent air in between the sample and the prism.

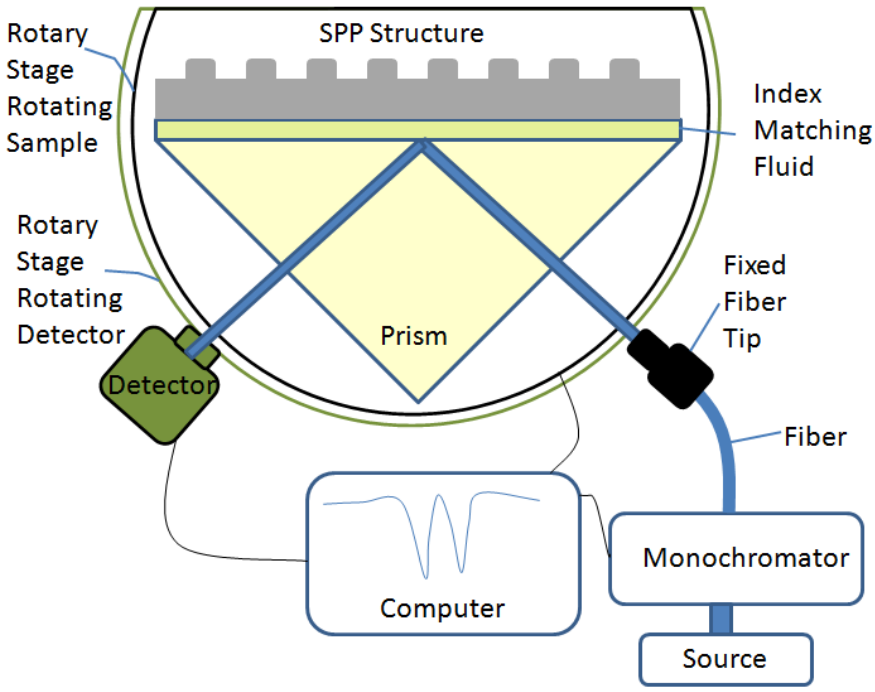

Figure 3.6: Schematic representation of an ellipsometer set up for reflection measurements.

Measurements are done with ellipsometer (Woollam, W-VASE32). Monochromator (HS-190) connected to a white light source (Xenon lamp) and quasi-monochromatic light is acquired to be used in ellipsometer for reflection measurements. Light is coupled to a fiber optic cable and made incident on the sample as a polarized and collimated beam. The sample is aligned in all directions on the sample stage at a selected angle to coincide the reflected beam into the detector. A base line is acquired from the lamp without any sample. White light from the fiber is reflected from the sample and fall onto the detector. Rotary stage change the incident angle and all wavelengths are scanned on the sample and reflected intensity is measured. The intensity spectrum is corrected using the base line. This procedure is repeated for different incidence angles and a dispersion curves are constructed with the help of a MATLAB program. Sample dispersion curves are given in Chapter 4.

Chapter 4

4. Phase Shifted Grating Based Plasmonic Cavities

This chapter is about the properties of SPPs in the plasmonic band gap cavities on uniform gratings and phase shifted gratings. Experimental and simulation results of SPP structures are given and compared. The role of grating ridge height on the plasmonic band gap formation has been studied .We find that the width of the band gap is linearly proportional to the grating ridge height. We also studied the effect of ridge width on the plasmonic band gap. We find that there is an optimum ridge width to observe the band gap. The dependence of the cavity state energy on the amount of phase shift in phase shifted gratings and higher order plasmonic band gaps are explained. The mechanism of SPP propagation on coupled phase shifted gratings is discussed. Strongly coupled cavity regime and weakly coupled cavity regimes are identified. The energy width of the cavity state has been studied as a function of cavity-to-cavity coupling.

4.1. Uniform Grating Based Plasmonic Band Gap

Uniform metallic gratings change the dispersion properties of SPPs on flat metal surfaces due to the interaction of SPPs with the periodic structure. Corrugations behave as scattering centers for SPPs [45]. Periodicity in the corrugation results in a forbidden energy gap to be formed in a specific frequency range which is related to the periodicity of the corrugations [26]. This energy band gap occurs when SPP momentum satisfies the Bragg condition

$$k_{SPP}=G/2 \tag{4.1}$$

where *G (G=2π/grating period)* is the reciprocal lattice vector.

We fabricated and characterized gratings with uniform periodicity using e-beam lithography to observe plasmonic band gap in the interval where Bragg condition is satisfied. The uniform grating is created with electron beam lithography having a period of 420 nm, a line width of 150 nm and a ridge height of 25 nm. The sample is prepared with the fabrication process which was discussed in Chapter 3. A thin glass is used as the template to produce metallic gratings, and 35 nm of silver is evaporated onto the glass slide in the box coater. Sample is coated with two kinds of PMMA for bilayer process with different molecular weights and thicknesses. Sample is soft baked in convection oven at 170° C for 20 minutes. A CamScan CS3200 electron lithography machine is used for electron beam lithography process, and 1 nanocoulomb line dose is exposed at 15 kV on the sample to form uniform grating on an area of 1.5 mm^2 with 14x14 small field sizes of 100μm^2 each. Sample is developed in 1:2 MIBK:IPA for 70 seconds and then washed in DI. 25 nm of silver is evaporated at box coater. Lift off process is achieved in hot acetone; all metal left on PMMA is lifted off. Sample is checked for the line widths and periods and defects under the SEM. Sample with very low defect density can be obtained frequently. SEM image of the structure is shown in figure 4.1. The

characterization is done with polarization dependent reflection measurements with the configuration discussed in Chapter 3 Fig. 3.9. The sample was mounted on the base of a prism as the grating side up with the help of index matching fluid coated in between the sample and the prism. The prism has a refractive index of 1.43 giving the enhancement to the momentum of light incident from below the grating with the configuration as shown in Fig. 3.9.

The prism coupler allows incoming photons to excite plasmons. Coupling can only be achieved when momentum of incident light with SPPs are matched. This matching condition is given as

$$k_{spp}=n_p k_0 sin(\theta)= n_p 2\pi\ sin(\theta)/\lambda_0 \quad (4.2)$$

where k_{spp} is the momentum of SPP, n_p is the refractive index of the prism, k_0 is the momentum of incident light, λ_0 is the wavelength of incident light and θ is the incidence angle. The dispersion curves for bound SPP modes in the visible and near infrared regime are created measuring coupling wavelength and incidence angle. A V-WASE32 ellipsometer is used for reflection measurements. Reflection spectrum of the uniform grating is shown in Fig. 4.2. The reflection measurements at different angles and wavelength of incident light results in two dimensional reflectivity map. Such a reflectivity map as represented in Fig. 4.2. Horizontal axis is the angle of incidence, it is proportional to momentum of SPP. Vertical axis is the wavelength of the incident light, and it is proportional to the energy of the SPP. Blue regions on the graph show the reflection minima where SPP is excited. Red regions represent the reflection maxima.

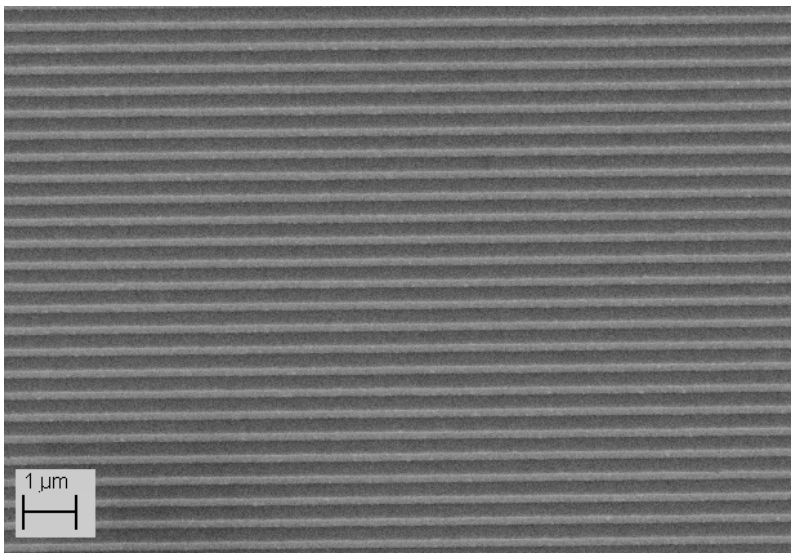

Figure 4.1: SEM image of a uniform grating with a period of 420 nm.

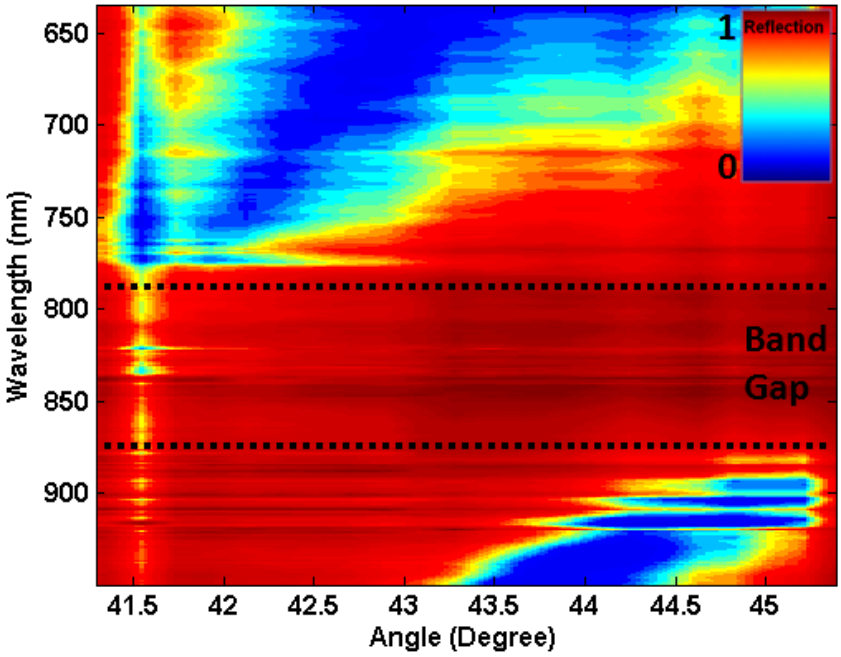

Figure 4.2: Dispersion of SPPs for the uniform grating with a period of 420 nm measured by reflectometer in the bound SPP mode regime.

Dispersion curve of the SPPs for the uniform grating plasmonic structure shows a band gap is opened up in between the 770 nm and 880 nm. SPP interacts with the periodic surface and Bragg scattering results in both forward and backward traveling waves that interfere constructively forming a standing wave profile. Two standing waves ω+ and ω- are at different energies. Energy of the ω+ is about 765 nm and energy of the ω- is about 885 nm. There are no plasmonic modes in n the band gap and ω+ localizes on the troughs and ω- localizes on the peaks of the grating as represented in Fig. 4.5. Within the band gap, SPPs destructively interfere and no SPP propagation is allowed in this range [26]. Life time of the plasmon increases as the energy of the SPPs decrease, due to decreasing penetration depths of plasmonic modes into the metal for lower frequencies [47]. High energy plasmonic modes penetrate deeper into the metal and this increases metallic loses that causes the life time of the plasmon to decrease. Our data supports this. This effect is checked by the line width of the reflection minima taken from a line scan at a constant coupling angle. [48]. Line widths of the plasmonic modes are wider above the band gap compared to line widths of the plasmonic modes below the band gap.

In order to verify these results numerically, the dispersion curve in Fig. 4.3 is calculated in plane wave source configuration. There is good agreement in dispersion profiles of uniform gratings between experiment and simulation. However, the width of the plasmonic modes obtained from simulation is narrower that those obtained from experiments due to the imperfect line shape of the ridges in the grating and rough surface of the silver film. Linewidths are interpreted in Fig. 4.4; line width of higher energetic SPP mode is wider than the lower energetic SPP mode. L1 is wider than L2.

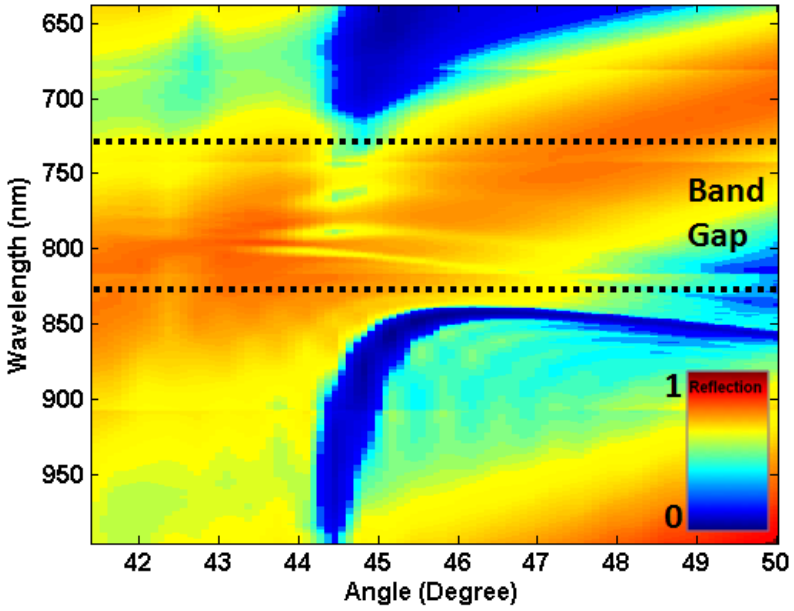

Figure 4.3: Dispersion of SPPs for the uniform grating with a period of 400 nm calculated in the bound SPP mode regime.

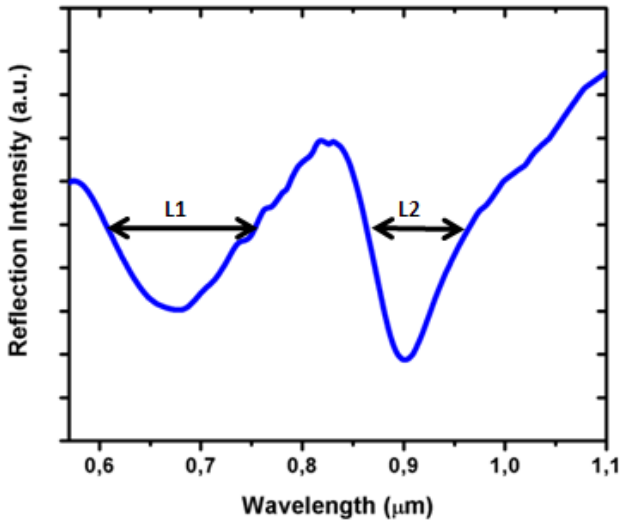

Figure 4.4: Width of the Reflection spectra of a uniform square grating with a period of 400 nm, SPP modes are excited at a 44.7^0 incidence angle and incident wavelength is varied.

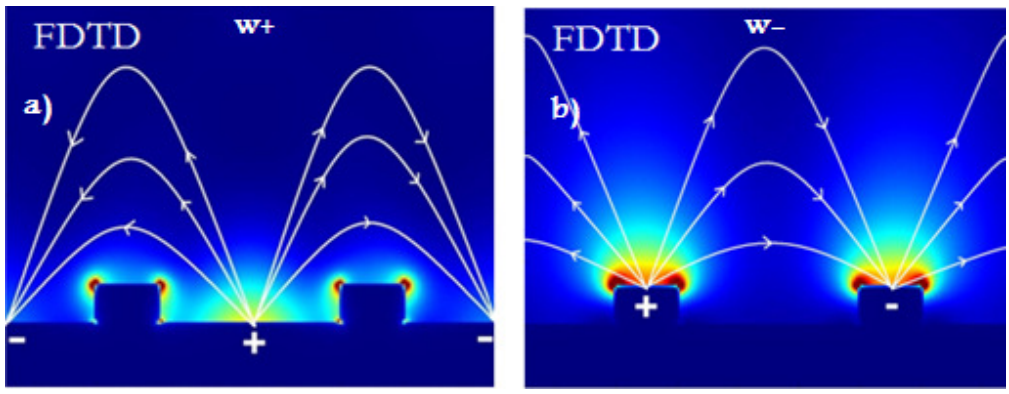

Figure 4.5: Electric field intensities and directions for a) ω+ and ω-.

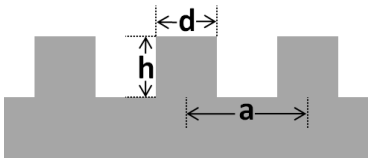

Figure 4.6: Schematic representation of a uniform square grating, a is the period, h is the ridge height, d is the ridge width and d/a is the duty cycle.

The width of the band gap is related to the energy of the upper and lower branches of SPP modes near the band gap edges. Energy of the ω+ and ω- is related to the distortion in electric field lines. Distortion in the electric field lines depends on the grating ridge height. The height of the ridges has a contribution to the energy of ω+ mode and has a small contribution of the energy of ω-, mode because height of the ridges distorts electric field lines of ω+ mode more than ω- mode. Therefore, as the grating ridge height increases, we expect for the band gap to be widened as shown in Fig. 4.7 [46].

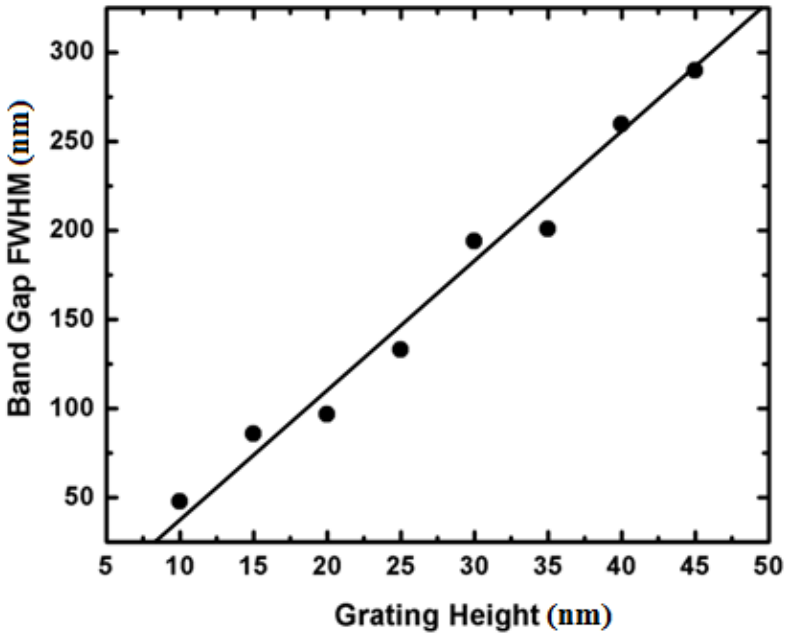

Figure 4.7: Modulation of plasmonic band gap with grating ridge height.

To have a better understanding of grating profile dependence of the band gap, width of the band gap must be characterized as a function of ridge height (h) and width (d) [or duty cycle (d/a)] of the grating must be tuned to observe the band gap. The parameters are labeled in Fig. 4.6. In the simulation set up that is used to calculate the energies of SPP modes supported by the plasmonic structure, a mode source is placed at the metal-air interface to launch the SPPs at the metal-dielectric interface. Reflected SPP is measured. The dip in the extinction data gives us the band gap of the plasmonic structure. The simulated structure has a period of 400 nm and a line width of 200 nm; ridge height of the grating is modulated in the range of 10 nm – 45 nm and extinction is calculated. Full width at half maximum of the extinction dip is calculated by changing the grating height. The band gap is opened up around 810 nm. The high energy edge ω+ mode moves to higher energies (blue shift) as the grating height is increased. Band gap modulation with grating height is given in Fig. 4.7. We conclude that the width of the plasmonic band gap widens as the

grating ridge height increases. In this way, the band gap can be tuned from 50 nm to 300 nm by changing the height of the grating from 10 nm to 45 nm for a metallic grating with period of 400 nm. Dependence of the band gap width on the grating ridge height is almost linear in this regime as seen in Fig. 4.7.

The width of the ridges also has effect on the plasmonic band gap. There is an optimum extinction depth that depends on the duty cycle. Extinction depth dependence on the ridge width is calculated in the SPP mode configuration. Extinction is calculated by modulating the duty cycle of the grating profile. Duty cycle cannot exceed the period of the grating. Optimum band gap extinction depth is searched through a script program for the numerical calculations.

Fig. 4.8 represents the calculated plasmonic modes supported by the plasmonic structure for different duty cycles. The calculations are carried out in mode source configuration. Extinction depth is labeled on the figure. Extinction depths are different for different duty cycles.

Fig. 4.9 shows the band extinction depth dependence on the duty cycle, duty cycle is shown in Fig. 2.6 as d/a. Optimum duty cycle is half of the period, because ω+ modes and ω- modes are confined in the through and peaks. As the width of through (peaks) gets short (long) compared to the periodicity, localization and confinement of ω+ modes and ω- modes at through and peak respectively is not satisfied. To form a band gap, both ω+ modes and ω- modes have to be formed. These two resulting structures look like flat metal structures which do not show band gap formation.

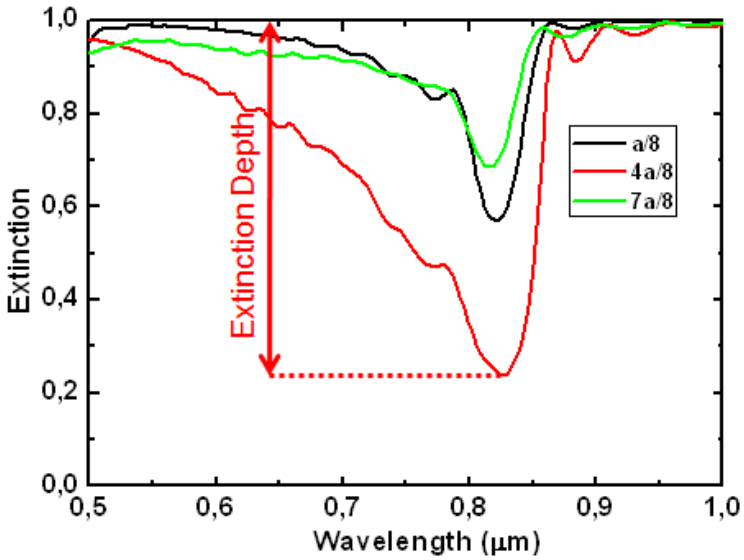

Figure 4.8: Graph of extinction vs. incident photon wavelength.

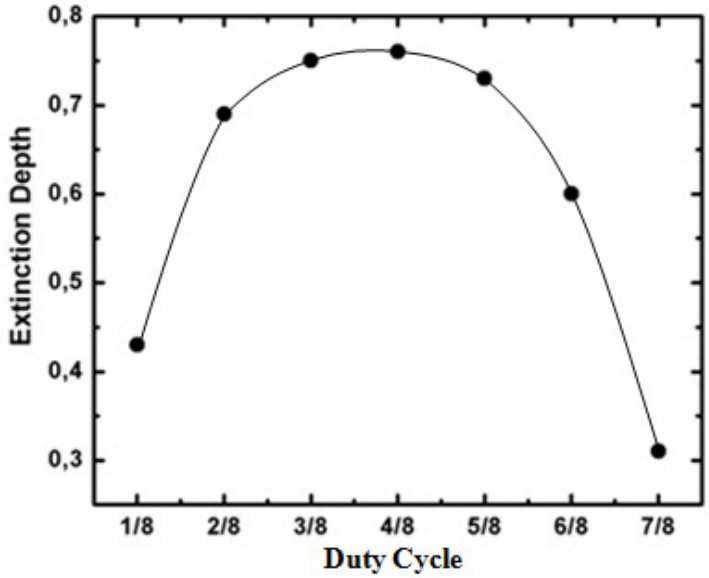

Figure 4.9: Graph of duty cycle vs. extinction depth.

4.2. Phase Shifted Grating Based Plasmonic Band Gaps and Cavities

Uniform metallic grating modifies the dispersion of SPPs on the flat metal surfaces due to interaction of SPP with the periodic structure. A band gap forms at a specific momentum and energy. Cavity states can be created by breaking the symmetry of the uniform metallic gratings. Transmission bands at energies within the band gap of the unperturbed grating are created [30]. New electromagnetic modes of cavities are created by constructive interference of the plasmons in the cavity. Interference maxima in the cavity region result in the SPP localization. Resonance condition is given by

$$\delta=(2n+1)\ (\lambda_{SPP}/4) \tag{4.3}$$

where δ is the phase shift added to the period of the uniform grating, n is the order of the cavity and a positive integer starting from zero, λ_{SPP} is the wavelength of the SPP.

The SBM structure that we fabricated to study the cavity formation consists of a phase shift at every 10 ridges with a period of 410 nm, a line width of 150 nm. A grating structure with phase shift of $\delta=\pi$ (205 nm– half of the period) is created with the use of e-beam lithography. The lithography process and measurement process is same with the processes mentioned in Chapter 4 to fabricate the grating and to acquire dispersion curve. SEM image of the SBM structure is shown in Fig. 4.10. The dispersion relation is shown in Fig. 4.11. Horizontal axis is the angle of incidence light which is proportional to momentum of incident light. Vertical axis is the wavelength of the incident light which is inversely proportional to the energy of the incident light. Blue regions on the graph show the reflection minima where SPPs are excited. Red regions represent the reflection maxima. A plasmonic cavity

state is created at approximately 820 nm. Quality factor is a dimensionless parameter defining the life time of the SPP cavity mode. Quality factor can be defined as the energy stored in the cavity over power loss from the cavity. It defines the life time of the cavity mode. It is calculated with dividing the center of the cavity peak frequency with FWHM of the cavity peak. Q-factor of the measured cavity is 82 which is good despite imperfect line shapes and roughness of the surface. The gap can be identified in between 740 and 890 nm. Cavity state is in the middle of the band gap, because of the π phase shift of SBM experienced by the SPPs. From Fig. 4.11, it is clear that the slope of the cavity state defines a standing wave.

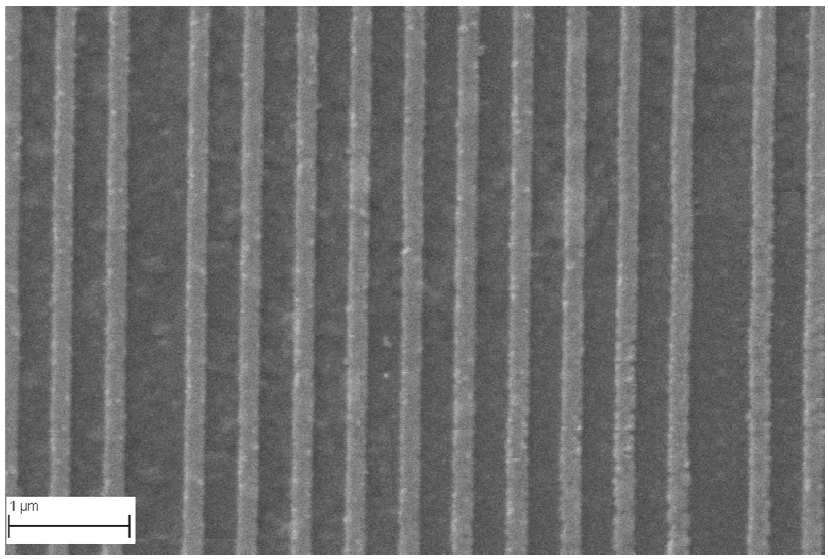

Figure 4.10: SEM image of a SBM with a period of 410 nm.

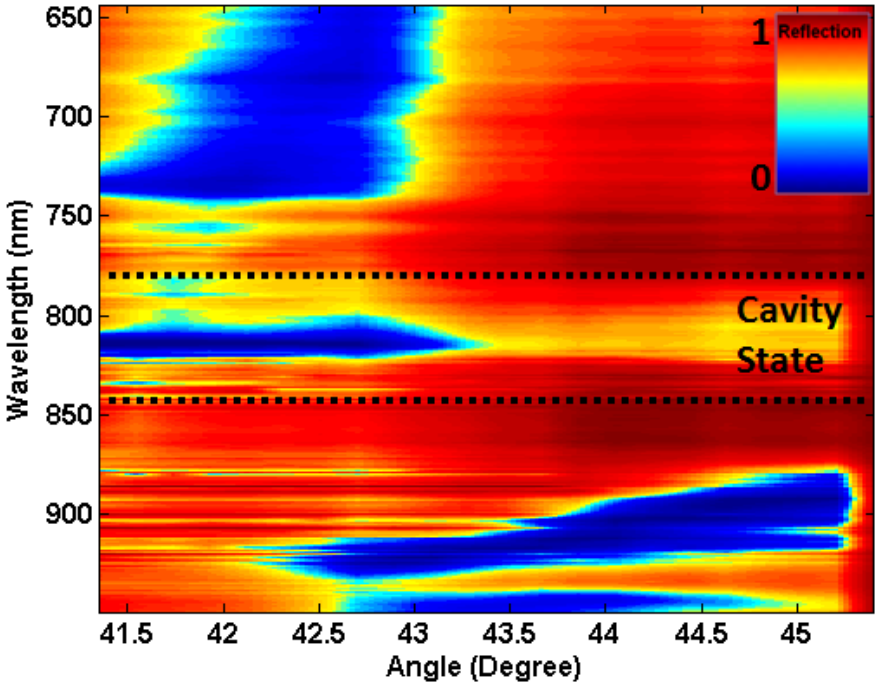

Figure 4.11: Dispersion for the SBM with a period of 410 nm measured by ellipsometer.

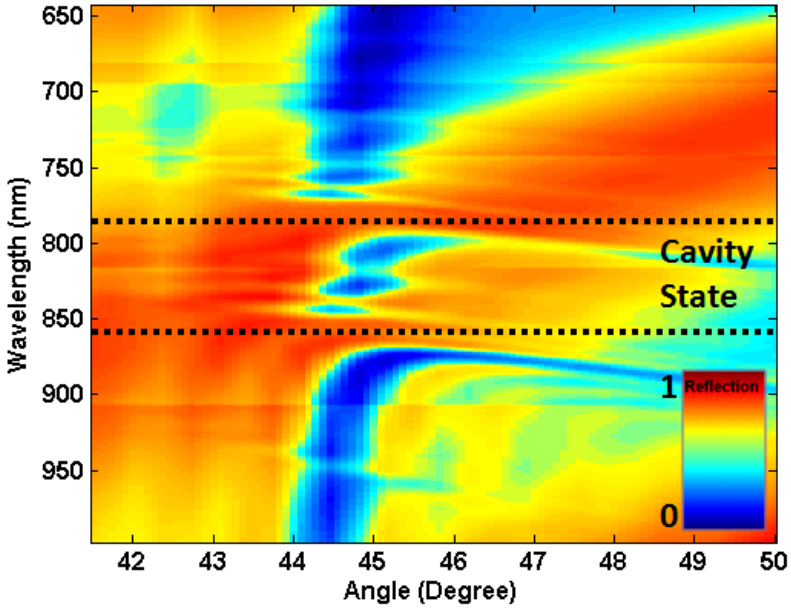

Figure 4.12: Dispersion for the uniform grating with a period of 400 nm calculated.

To understand the experimentally acquired dispersion curves we simulated the dispersion curve for SBM structures with a structure consisting of a phase shift at every 10 ridges with a period of 400 nm, line width of 200 nm (duty cycle 50%) and a phase shift of $\delta=\pi$ is in plane wave source configuration. In the simulation results shown in Fig. 4.12, we find that a cavity state is formed between the band edges of 790 nm and 850 nm. The dispersion profiles of experimental and numerical results are in close agreement; both have lower energy branch, ω-, at approximately 880 nm and upper energy branch, ω+, at approximately 750 nm and a cavity state within these branches are formed.

To see how SPP cavity mode localizes at cavity structures, electric field intensity profiles of cavity modes have been calculated. The cavity structure was achieved by adding a phase shift of π to the period of the uniform grating periodically after every ten ridges. Cavity states supported by the SBM are calculated using the plane wave configuration.

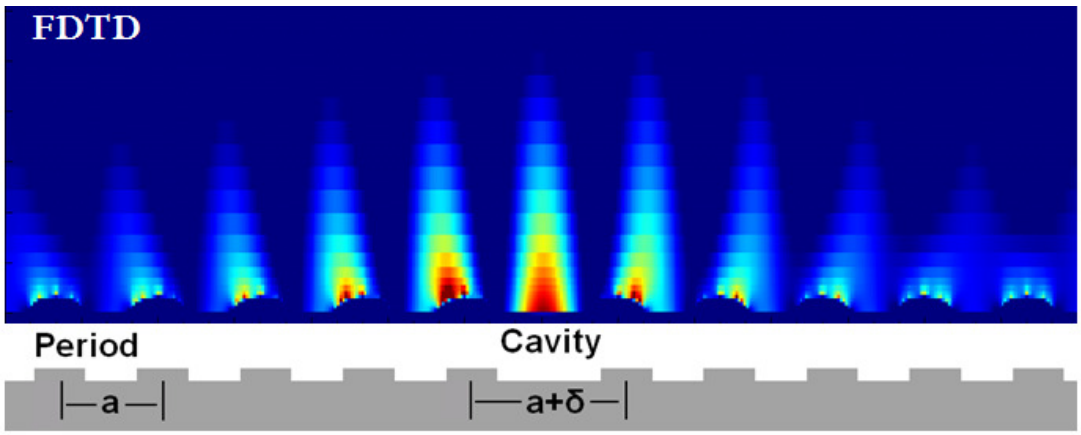

Figure 4.13: Electric field intensity distribution of SPPs excited on a SBM with phase shifts of π.

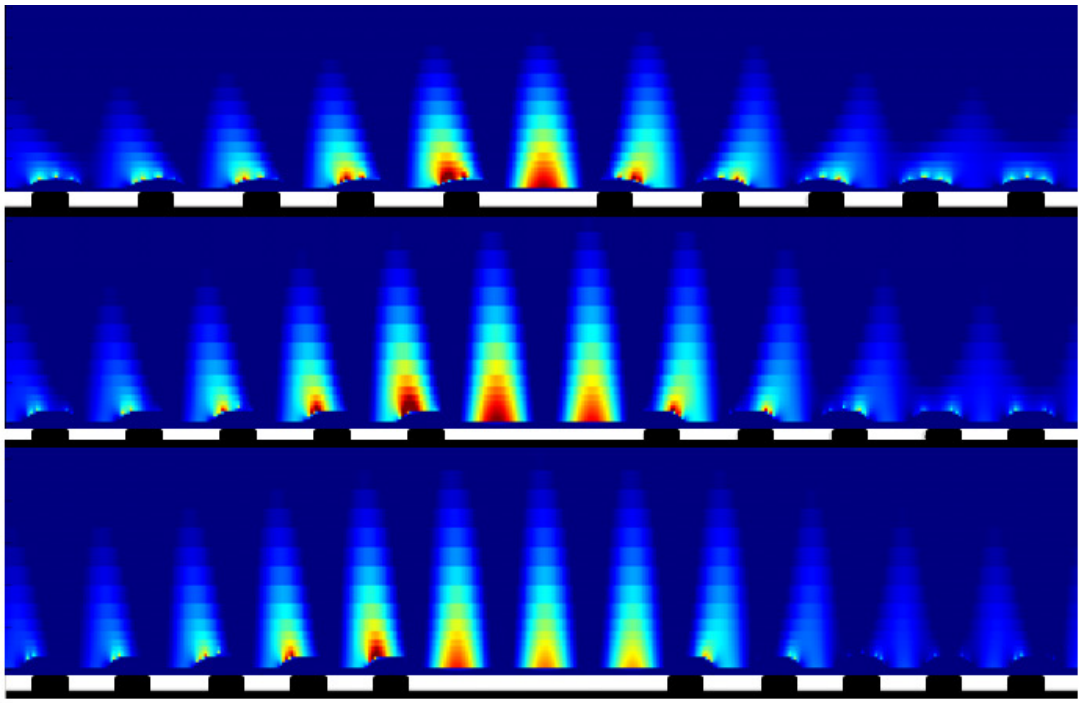

Figure 4.14: FDTD calculated electric field intensity distribution of SPPs excited on a SBM with phase shifts of π, 3π and 5π from top to bottom, respectively.

Electric field intensity distribution is shown in Fig. 4.13 for the SPP mode supported by the cavity. Electric field intensity distribution for the same resonance wavelength excited on SBMs with phase shifts of π (n=0), 3π (n=1) and 5π (n=2) from top to bottom respectively is shown in Fig. 4.14. A close look at the cavity region shows that one, two and three electric field peaks are located within the cavity regions for n=1,n=2,and n=3 modes respectively. These are excited at the resonant wavelengths of SPP modes supported by the SBM profiles. There are n+1 localized electric field peaks within each cavity region.

By controlling the phase properties of the SBM structure, resonance condition can be achieved and SPPs at energies within the band gap constructively interfere forming a localized SPP cavity mode within the cavity region. In Fig. 4.15 cavity the plasmonic modes for an SBM with a phase shifts are indicated with arrow. By adding a phase shift to the uniform grating, a new state is created within the band gap region in between the ω+ and ω- modes. Cavity state formation for SPP can also be explained as the constructive interference of SPPs for wavelengths within the band gap.

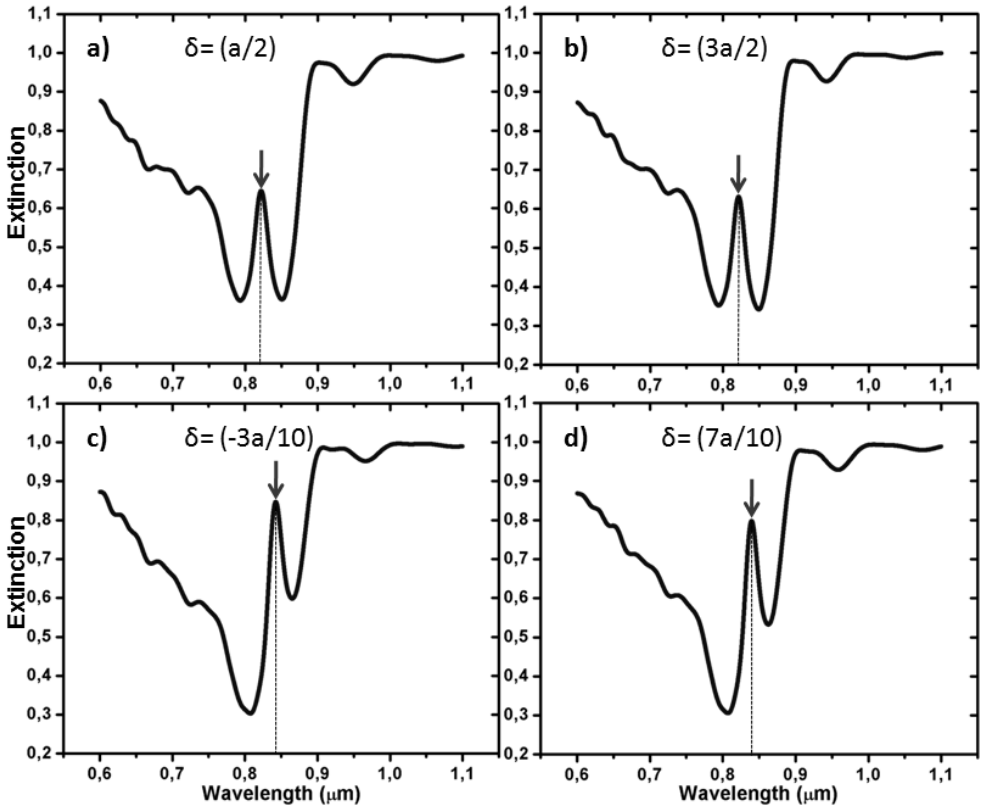

Figure 4.15: Extinction data for SBMs with a phase shift of δ a) a/2 times period b) 3a/2 times period b) -3a/10 times period b) 7a/10 times period.

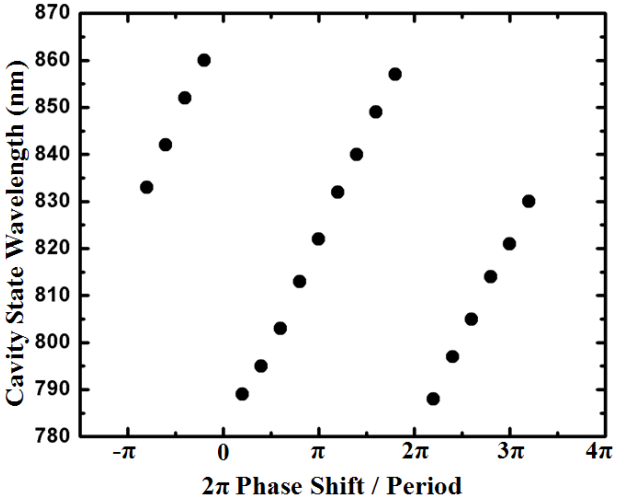

Figure 4.16: Graph of 2π times phase shift divided by period vs. cavity state.

In order to understand the energy of the cavity state dependence on phase shift, cavity state energy is characterized with modulating the phase shift. Fig. 4.15 shows the energies of SPP cavity modes with different phase shifts of δ. Energy of the cavity state depends on the phase shift of the SBM structure. Constructive interference within the band gap is related to phase shift and therefore, energy of the SPP cavity mode inside the band gap changes as the phase changes [30]. In Fig. 4.15, energies of the SPP cavity modes are the same for the phase shifts of δ= a/2 (π) and δ= 3a/2 (3π). There is 2π difference in between the phase shifts. Same phenomena is valid for energies of SPP cavity modes for the phase shifts of δ=-3a/10 (-3π/5) and δ= 7a/10 (7π/5). Fig. 4.16 shows the energy of the cavity state dependence to the phase shift of the SBM structure. Energy states of the cavities are almost the same for the phase shifts that undergoes after a round trip of 2π phase shift. This is interpreted in Fig. 4.16, cavity state energies are the same for 2π times phase shifts/periods of -0.8 π, 1.2 π and 3.2 π.

4.3. SPP Propagation Mechanism on Coupled Phase Shifted Gratings

High Q-factor optical cavities are obtained by breaking the symmetry of a photonic crystal [49]. High transmission bands at frequencies within the band gap of the uniform photonic crystal are created by the coupling of supported electromagnetic modes of cavities [28]. Overlap of the evanescent field of the modes supported by the adjacent cavities results in these band formations [50]. The propagation mechanism of light under these circumstances is known as the photon hopping from a given cavity to the next one [51].

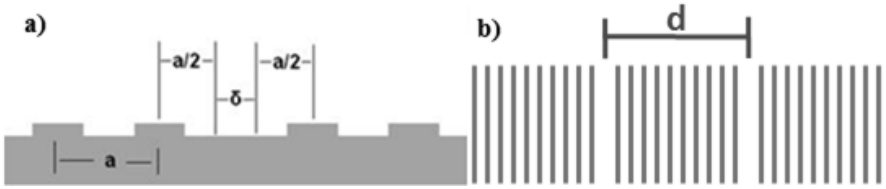

Figure 4.17: (a) Schematic side view of a cavity structure with a phase shift of δ. (b) Schematic side view of a sampled Bragg mirror (SBM) consisting of coupled SPP cavities.

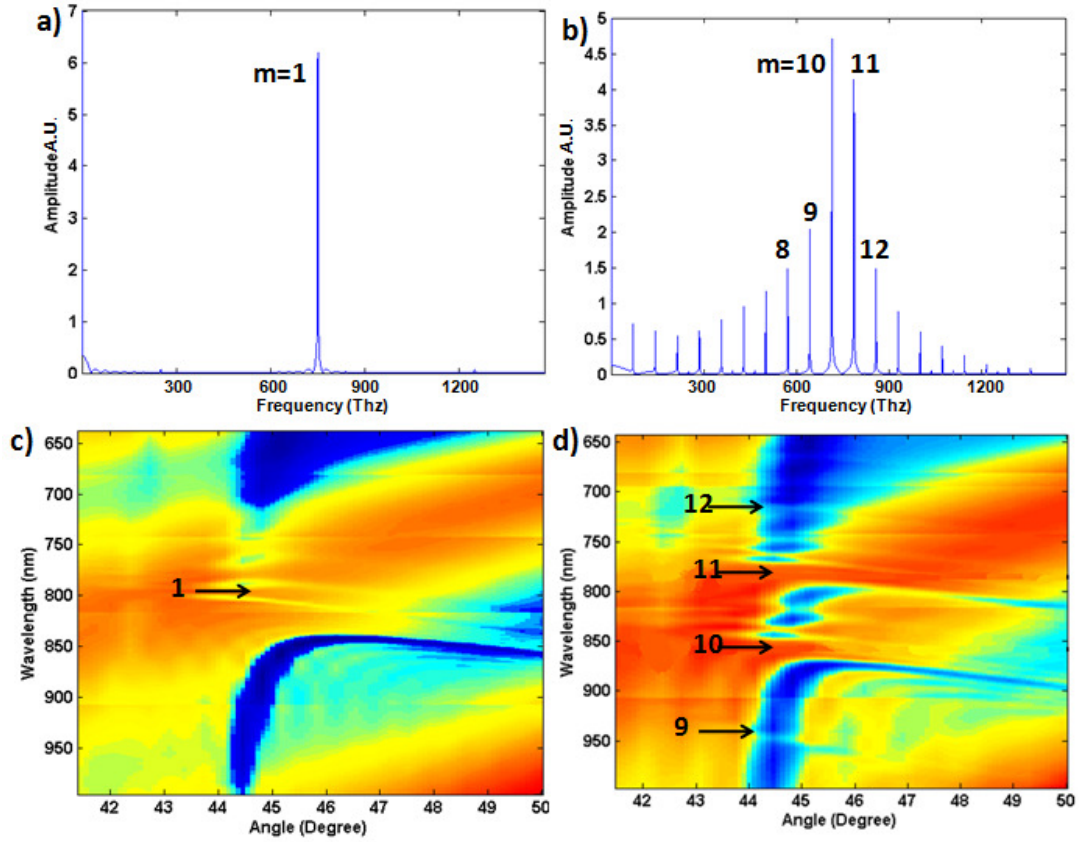

Figure 4.18: (a) Fast Fourier transform of the profile of the unperturbed grating. (b) Fast Fourier transform of the profile of the SBM. (c) Reflectivity of a silver grating that has silver ridges with a period a=400 nm, a line width=200 nm, a line height=30 nm. (d) Reflectivity of a silver SBM of silver ridges with a period a=400 nm, line width=200 nm, line height=30 nm.

The cavity structure that was studied is shown in Fig. 4.17 (a) and Fig. 4.17 (b). Each cavity is created by inserting a phase shift every N ridges. . The structure is composed of a thin layer of silver on a glass substrate with a grating profile and the phase shift element. Two adjacent gratings are separated by a phase shift. This generates a coplanar one dimensional SPP cavity [29, 30]. N is the number of ridges between the two adjacent cavities and the period of the SBM is given by

$$d=Na+\delta. \tag{4.4}$$

The uniform grating and SBM plasmonic modes are calculated with the plane wave configuration. The results are shown in Fig. 4.18 (c) and (d) for a uniform SPP grating ($\delta=0$) and in Fig. 4.18 (d) for a SBM. For a one dimensional silver grating, the SPP dispersion shows a 0.22 eV wide energy band gap centered around 800 nm at the boundary of the Bragg condition. For the SBM, the dispersion curve indicates two band gaps near the Bragg condition of the uniform grating. The reflectivity reveals SBM plasmon modes within the band gap of the unperturbed mirror. The properties of higher order gaps modes can be analyzed from the Bragg condition [49]. For a SPP traveling perpendicular to the silver ridges, a Bragg reflection occurs with the condition that

$$k_{SPP}=mG/2 \tag{4.5}$$

where k_{SPP} is in-plane phase constant of the bare thin film SPP and $G=2\pi/d$ is the reciprocal lattice vector of the SBM and m is the Fourier harmonic of the grating. The energy width for the band gap for a Bragg order m is linearly proportional to the magnitude of the Fourier harmonic of the grating with a frequency m/d [52]. If N is sufficiently large, the profile of the SBM is only little different from original grating since only 1/N period is perturbed. The largest Fourier harmonic amplitudes for SBM will be for m/d~1/a [49].

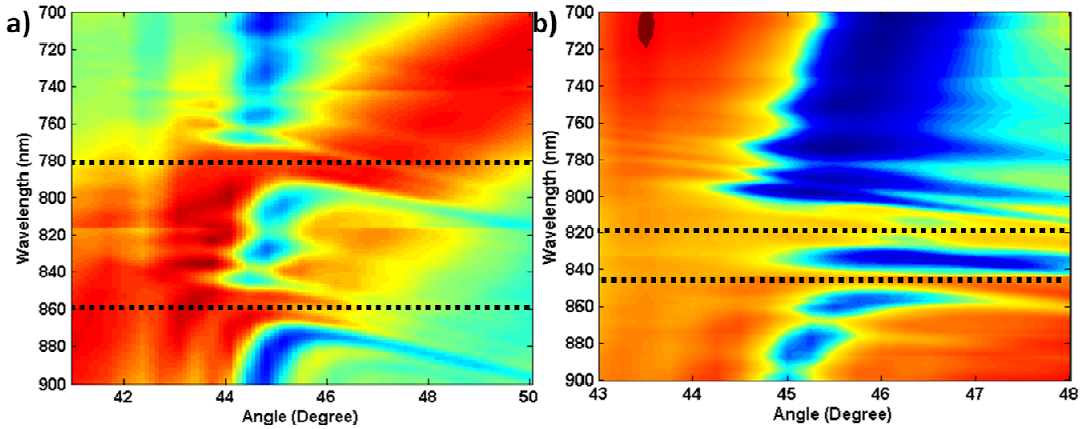

Figure 4.19: (a) Dispersion of SBM cavity that has 10 ridges in between each phase shift region. (b) Dispersion of SBM that has 30 grating lines in between each phase shift region.

The gaps observed in Fig. 4.18 (c) and (d) is in agreement with Bragg orders given by

$$m_1=N+\text{int}(\delta/a) \tag{4.6}$$

$$m_2=m_1+1$$

where int(δ/a) is the integer part of the δ/a. Fourier transform of the SBM shows two peaks m_1 and m_2. A cavity mode is resonant if

$$\delta=(2n+1)\,(\lambda_{SPP}/4) \tag{4.7}$$

which is at the gap energy of the uniform grating [29]. If resonant cavities are coupled, electromagnetic modes that are supported by cavities are observed within an energy band that is wider than the single cavity resonance and centers on it [50]. In Fig. 4.18 (c), the band observed which is centered on 825 nm is referred as the coupling of the SBM resonant cavities.

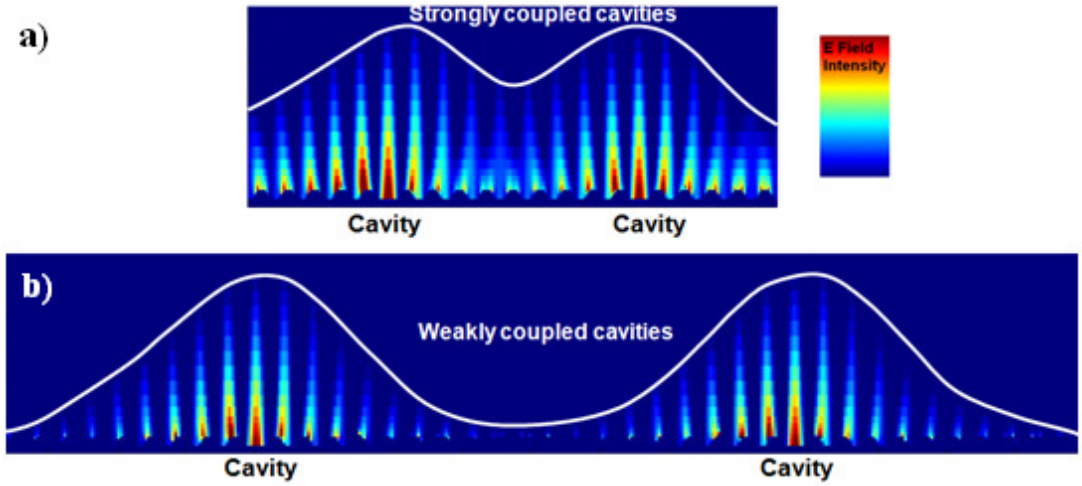

Figure 4.20: (a) Electromagnetic modes supported by cavities with a phase at every 10 ridges. Note the coupling of the cavities. (b) Electromagnetic modes supported by cavities with a phase shift at every 30 ridges.

Overlap of the electromagnetic modes supported by adjacent cavities are strongly coupled when they are near each other and they form a wide energy band within the band gap of uniform grating. When cavities are further apart from each other, they are weakly coupled and they form narrow energy band [53]. Fig. 4.19 (a) represents the dispersion curve for the SBM structure with a phase shift at every 10 ridges having a period of a=400 nm and a phase shift of δ=200 nm. We find that a wide band cavity mode is associated with this structure. Fig. 4.19 (b) represents the dispersion curve for the SBM structure with a phase shift at every 30 ridges having a period of a=400 nm and a phase shift of δ=200 nm. For this structure a narrow band cavity mode is identified which is more localized. Strong coupling and overlapping of modes supported by cavity for a SBM structure with a phase shift at every 10 ridges which is excited at the cavity mode having 825 nm light incident at 44.7 degree is shown in Fig. 4.20 (a). The evanescent tails of the modes are seen to overlap. Weakly coupling and overlapping of the modes supported by a SBM cavity for the with 30 ridges which is excited at the cavity mode having 825 nm light

incident at 46.3 degree is shown in Fig. 4.20 (b). The evanescent tail of the modes are observed to weakly overlap. Maxima in Fig. 4.20 (a) caused by the field enhancement inside the cavities and for energies within the gap are resonant and cavity state mode at this energy increases from hopping process.

Similar results are obtained by Dereux et.al [49]. In the work done by Dereux, the cavity-cavity coupling issue and hopping process is explained too. Electric field intensity profiles of cavity states are measured with the use of near field scanning optical microscope. We have obtained the same experimental intensity profiles in a numerically calculated way. Dereux just calculated the dispersion of SPPs at uniform grating and SBM with differential method. We have been able to measure the dispersion of such structures by producing large area samples. We have identified the weakly coupled and strongly coupled SPPs in different kind of SBMs.

Chapter 5

5. Conclusions

Uniform metallic gratings and SBM structures are fabricated using e-beam lithography onto the large area samples. These plasmonic structures are characterized by measuring the reflection data by the help of prism coupler method.

Experimentally obtained dispersion curve of the uniform metallic grating which is produced with the use of e-beam lithography indicates formation of band gap. Observation of the band gap is verified numerically.

Numerically, we find that the band gap width for SPPs highly depends on the grating height, as the grating height increases, the width of the band gap increases. There is an optimum width to observe band gap in periodic structure; optimum line width is half of the period.

Experimentally obtained dispersion curve of the SBM which is produced with the use of e-beam lithography indicates formation of a cavity mode within the band gap of the uniform grating. Observation of the cavity state is verified numerically.

Numerically, we observed that amount of phase shift added to the uniform grating defines where cavity state occur within the band gap of the uniform grating. Energy of the cavity state is periodic within the band gap related to the phase shift.

We find in numerical calculations that the cavity states at energies within the band gap of the uniform plasmonic crystal are created by the coupling of supported electromagnetic modes of cavities. Overlap of the evanescent field of the modes supported by adjacent cavities cause wide energy bands within the band gap. The propagation mechanism of SPP is plasmon hopping from a given cavity to the next one.

An application of cavity structures can be the use of SBMs as a template in SERS applications. A cavity state with the wavelength of the incident laser beam can be created in SBM structures. As an example, laser operating at 632 nm light can excite the plasmons with the use of a prism coupler on SBM structure such that the SBM structure consists of a period of 256 nm, a ridge width of 128 nm and a phase shift of π (128 nm) after every ten ridges. The structure is coated with a thick layer of PMMA (more than 3μm). PMMA layer includes dilute molecules to be sensed in SERS, it is dilute because the refractive index of PMMA layer should not be affected by the molecules dramatically. When the refractive index of this layer is 1.4, the laser light can excite the plasmons at cavity state. Decoupled light from SPPs can be collected with a lens from top of the grating to be sensed in SERS. It should be noted that the structure may have to be modified due to a change in the refractive index of the dielectric coating that is used on the metal surface to host the molecules to be studied with SERS as the concentration of molecules changes inside the PMMA layer. This is because, as the refractive index of the dielectric increases, cavity mode will shift to lower energies. With proper simulations and experimental verifications, such structures can be used in SERS.

Bibliography

1 – A. Sommerfeld, “Reproduction of electro-dynamic waves at a cylinder leader ", Ann. der Physik und Chemie, vol. 67, pp. 233–290, Dec 1899. (*Tr*.)

2 – J. Zenneck, *Ann. der Physik,* **23**, 846--866 (1907).

3 – U. Fano, “The Theory of Anomalous Diffraction Gratings and of Quasi-Stationary Waves on Metallic Surfaces (Sommerfeld’s Waves)” JOSA, Vol. 31, Issue 3, pp. 213-222 (1941)

4 – R. H. Ritchie “Plasma Losses by Fast Electrons in Thin Films” Phys. Rev. 106, 874–881 (1957)

5 - E. *Kretschmann*, H. *Raether*, "Radiative decay of nonradiative surface plasmons excited by light," Z. Naturforsch. A. 23, 2135-2136 (*1968*)

6 - Born, Max, E. Wolf. *Principles of Optics*. Cambridge University Press, (1997)

7 – WL Barnes, A Dereux, and TW Ebbesen. “Surface Plasmon Subwavelength Optics” Nature, 424 (6950):824-830, AUG 14 2003

8 - Fleischmann, M. PJ Hendra and AJ Mc Quillan (15 May 1974). "Raman Spectra of Pyridine Adsorbed at a Silver Electrode". *Chemical Physics Letters* **26** (2): 163–166.

9 - Nie, S. Emory, S. R. "Probing Single Molecules and Single Nanoparticles by Surface-Enhanced Raman Scattering" Science 1997, 275, (5303), 1102-1106.

10 - Yun-Tzu Chang, Yueh-Chun Lai, Chung-Tien Li, Cheng-Kuang Chen, and Ta-Jen Yen "A multi-functional plasmonic biosensor" Optics Express, Vol. 18, Issue 9, pp. 9561-9569 (2010).

11- Rupert F. Oulton, Volker J. Sorger, Thomas Zentgraf, Ren-Min Ma, Christopher Gladden, Lun Dai, Guy Bartal & Xiang Zhang "Plasmon lasers at deep subwavelength scale" *Nature,* 2009*,* 461, 629-632.

12 – G. Mie, "Contributions to the Optics of Turbid Media, Particularly of Colloidal Metal Solutions" Leipzig, *Ann. Phys.* 330 377-445 (1908)

13 – Stefan Alexander Maier "Plasmonics Fundamentals and Applications" (Springer, New York, NY, 2007).

14 – M.E. Stewart, C.R. Anderson, L.B. Thompson, J. Maria, S.K. Gray, J.A. Rogers, and R.G. Nuzzo, "Nanostructured Plasmonic Sensors" Chem. Rev. 108, 494-521 (2008)

15 – W.A. Murray, and W.L. Barnes "Plasmonic Materials" Adv. Matter, 19, 3771-3782 (2007)

16 - Ivan H. El-Sayed, Xiaohua Huang, and Mostafa A. El-Sayed "Surface Plasmon Resonance Scattering and Absorption of anti-EGFR Antibody Conjugated Gold Nanoparticles in Cancer Diagnostics: Applications in Oral Cancer" *Nano Lett.*, 2005, 5 (5), pp 829–834

17 - Koichi Okamoto, Isamu Niki, Alexander Shvartser, Yukio Narukawa, Takashi Mukai & Axel Scherer, “Surface-plasmon-enhanced light emitters based on InGaN quantum wells” Nature Materials 3, 601 - 605 (2004)

18 – Harry A. Atwater and Albert Polman “Plasmonics for improved photovoltaic devices” Nature Materials 9, 205 (2010)

19 – T. W. Ebbesen, H. F. Ghaemi, Tineke Thio, D. E. Grupp, H. J. Lezec, “Surface plasmons enhance optical transmission through subwavelength holes” Phys. Rev. B 58, 6779–6782 (1998)

20 – M. Quinten, A. Leitner, J. R. Krenn, and F. R. Aussenegg “Electromagnetic energy transport via linear chains of silver nanoparticles” Optics Letters, Vol. 23, Issue 17, pp. 1331-1333 (1998)

21 - E. Verhagen, A. Polman and L. Kuipers “Nanofocusing in laterally tapered plasmonic waveguides” Optics Express **16**, 45 (2008)

22 – Nicholas Fang, Hyesog Lee, Cheng Sun, Xiang Zhang “Sub–Diffraction-Limited Optical Imaging with a Silver Superlens” Science, Vol. 308. no. 5721, pp. 534 – 537 (2005)

23 – Yoichi Kurokawa and Hideki T. Miyazaki “Metal-insulator-metal plasmon nanocavities: Analysis of optical properties” Phys. Rev. B 75, 035411 (2007)

24 – Amir Hossieni and Yehia Massoud “A low-loss metal-insulator-metal plasmonic bragg reflector” Optics Express, Vol. 14, Issue 23, pp. 11318-11323 (2006)

25 - J. D. Joannopoulos, R. D. Meade, and J. N. Winn, *Photonic Crystals* (Princeton University Press, New Jersey, 1995).

26 - W. L. Barnes, T. W. Preist, S. C. Kitson, and J. R. Sambles “Physical origin of photonic energy gaps in the propagation of surface SPPs on gratings” Physical Review B, Volume 54, Number 9, 6227-6244 (1996).

27 – E. Yablonovitch, T.J. Gmitter, R.D. Meade, A.M. Rappe, K.D. Brommer and J.D. Joannopoulos “Donor and acceptor modes in photonic band structure” Phys.Rev.Lett. 67, 3380 (1991).

28 – Mehmet Bayindir, B. Temelkuran, and E. Ozbay “Tight-Binding Description of the Coupled Defect Modes in Three-Dimensional Photonic Crystals” Phys. Rev. Lett. 84, 2140–2143 (2000).

29 - J.-C. Weeber, A. Bouhelier, G. Colas des Francs, L. Markey, and A. Dereux “Submicrometer In-Plane Integrated Surface Plasmon Cavities” *Nano Lett.*, **2007**, *7* (5), pp 1352–1359.

30- Yiyang Gonga and Jelena Vučković “Design of plasmon cavities for solid-state cavity quantum electrodynamics applications” Applied Physics Letters, 90, 033113 (2007).

31 - A. Kocabas, S. S. Senlik, and A. Aydinli, “Slowing down surface SPPs on a moiré surface,” Phys. Rev. Lett. 102(6), 063901 (2009).

32 - A. Kocabas, S. S. Senlik, and A. Aydinli, “Plasmonic band gap cavities on biharmonic gratings”, Phys. Rev. B. **77**, 195130-1-195130-7 (2009).

33 - Mark Fox, *Optical Properties of Solids*, Oxford University Press, USA 2006

34 - Alexandre Vial, Anne-Sophie Grimault, Demetrio Macías, Dominique Barchiesi, and Marc Lamydela Chapelle “Improved analytical fit of gold dispersion:

Application to the modeling of extinction spectra with a finite difference time domain method" Physical Review B 71, 085416 (2005)

35 - A. R. Zakharian, J. V. Moloney, and M. Mansuripur, "Surface plasmon polaritons on metallic surfaces," Opt. Express **15**, 183-197 (2007).

36 – Stefan A. Maier, Michelle D. Friedman, Paul E. Barclay and Oskar Painte, "Experimental demonstration of fiber-accessible metal nanoparticle plasmon waveguides for planar energy guiding and sensing" Applied Physics Letters 86, 071103 (2005)

37 – Amnon Yariv, Yong Xu, Reginald K. Lee, and Axel Scherer "Coupled-resonator optical waveguide: A proposal and analysis" June 1, Vol.24, No.11 Optics Letters (1999).

38 – Kane Yee "Numerical solution of initial boundary value problems involving Maxwell's equations in isotropic media" Antennas and Propagation, IEEE Transactions on Antennas and Propagation May 1966 Volume: 14 Issue: 3 On page(s): 302 - 307 (1966).

39 - McCord, M. A.; M. J. Rooks (2000). SPIE, Handbook of Microlithography, Micromachining and Microfabrication.

40 - http://www.museumstuff.com/learn/topics/electron_beam_lithography

41 - http://www.camscan.com/cs3000

42 - http://www.microchem.com/products/pdf/PMMA_Data_Sheet.pdf

43 - http://www.rp-photonics.com/supercontinuum_generation.html

44 - http://micro.magnet.fsu.edu/primer/java/filters/aotf/index.html

45 - Martin Kuttge, F. Javier García de Abajo, and Albert Polman “How ridges reflect and confine surface plasmon polaritons” Optics Express 17, 10385 (2009).

46 – B. Fischer, T. M. Fischer, and W. Knollb “Dispersion of surface-plasmons in rectangular, sinusoidal, and incoherent silver gratings” J. Appl. Phys. **75**, 1577 (1994).

47 – William L. Barnes “Surface plasmon–polariton length scales: a route to sub-wavelength optics” J. Opt. A: Pure Appl. Opt. 8 (2006) S87–S93.

48 – V.M. Silkin and E.V. Chulkov “Energy and lifetime of surface plasmon from first-principles calculations” Vacuum 81 (2006) 186–191.

49 – J.-C. Weeber, A. Bouhelier, G. Colasdes Francs, S. Massenot, J. Grandidier, L. Markey and A. Dereux “Surface-plasmon hopping along coupled coplanar cavities” PHYSICAL REVIEW B 76,113405 (2007).

50 – N. Stefanou, A. Modinos “Impurity bands in photonic insulators” Phys. Rev. B 57, 12127–12133 (1998).

51 - A. Yariv, Y. Xu, R. K. Lee, and A. Scherer, ″Coupled-resonator optical waveguide: a proposal and analysis,″ Opt. Lett. 24711 (1999).

52 - A. Yariv and P. Yeh, “Optical Waves in Crystals” (Wiley-Interscience, Hoboken, NJ, (2003).

53 – Sinan Balci, Mustafa Karabiyik, Askin Kocabas, Coskun Kocabas and Atilla Aydinli, “Coupled Plasmonic Cavities on Moiré Surfaces” Plasmonics, 10.1007/s11468-010-9161-8 (2010)

54 – Handbook of Optical Constants of Solids, Edward D. Palik. Academic Press, Boston, 1985

55 – www.lumerical.com

56 - http://www.wave-scattering.com/drudefit.html